

CHEMOUT: CHEMical complexity in star-forming regions of the OUTER Galaxy

V. Chemical composition gradients as a function of the galactocentric radius

D. Gigli^{1,2}, F. Fontani^{1,3,4}, L. Colzi⁵, G. Vermariën⁶, S. Viti^{6,7,8}, V. M. Rivilla⁵, and A. Sánchez-Monge^{9,10}

¹ INAF - Osservatorio Astrofisico di Arcetri, Largo E. Fermi 5, I-50125, Florence, Italy
e-mail: diegogigli.dg@gmail.com

² Dipartimento di Fisica e Astronomia, Università di Firenze, Via G. Sansone 1, 50019 Sesto Fiorentino, Firenze (Italy)

³ Max-Planck-Institut für extraterrestrische Physik, Giessenbachstraße 1, 85748 Garching bei München, Germany

⁴ LUX, Observatoire de Paris, PSL Research University, CNRS, Sorbonne Université, F-92190 Meudon, France

⁵ Centro de Astrobiología (CAB), CSIC-INTA, Ctra. de Ajalvir Km. 4, 28850, Torrejón de Ardoz, Madrid, Spain

⁶ Leiden Observatory, Leiden University, PO Box 9513, 2300 RA Leiden, The Netherlands

⁷ Transdisciplinary Research Area (TRA) 'Matter'/Argelander-Institut für Astronomie, University of Bonn, Bonn, Germany

⁸ Department of Physics and Astronomy, University College London, Gower Street, London, UK

⁹ Institut de Ciències de l'Espai (ICE), CSIC, Campus UAB, Carrer de Can Magrans s/n, 08193 Bellaterra (Barcelona), Spain

¹⁰ Institut d'Estudis Espacials de Catalunya (IEEC), 08860, Castelldefels (Barcelona), Spain

Received 15 June 2025 / Accepted 16 September 2025

ABSTRACT

Context. The outer Galaxy is characterized by lower metallicity compared to regions near the Sun, which suggests that the formation and survival of molecules in star-forming regions within the inner and outer Galaxy are likely to be different.

Aims. To understand how chemistry evolves across the Milky Way, deriving molecular abundances in star-forming regions in the outer Galaxy is essential to refining chemical models designed for environments with subsolar metallicity.

Methods. We analyzed IRAM 30 m observations in several spectral windows at 3 and 2 mm, toward a sample of 35 sources located at galactocentric distances of $\sim 9 - 24$ kpc in the context of the project CHEMical complexity in star-forming regions of the outer Galaxy (CHEMOUT).

Results. We focused on the species that have the highest detection rate (i.e., HCN, HCO⁺, *c*-C₃H₂, H¹³CO⁺, HCO, and SO), and searched for possible trends in column densities, abundances, and line widths with the galactocentric distance. We also updated the abundances for H₂CO and CH₃OH, presented in a previous work, using H₂ column densities from new NIKA2 dust continuum maps. The fractional abundances with respect to H₂ of most of the species (i.e., HCN, HCO⁺, *c*-C₃H₂, HCO, H₂CO, and CH₃OH) scale at most as the elemental fractional abundance of carbon ([C/H]) up to the investigated galactocentric distance of ~ 24 kpc. For the abundances of SO, we find a steeper gradient than that of sulfur elemental abundance ([S/H]). In contrast, the abundances of H¹³CO⁺ exhibit a shallower gradient relative to that of [¹³C/H]. Interestingly, we find that gas turbulence, as derived from the full width at half maximum of the lines, decreases with galactocentric distance for all the species investigated, suggesting a more quiescent environment in the outer Galaxy.

Conclusions. These results suggest that, in the outer Galaxy, the efficiency in the formation of most of the molecules studied, scaling with the availability of the parent element, is at least as high as in the local Galaxy, or perhaps even higher (e.g., for H¹³CO⁺). Yet, other species, such as SO, are characterized by a lower formation efficiency. These outcomes have important implications for the chemistry occurring in the outermost star-forming regions of the Galaxy and can help to constrain models adapted to lower metallicity environments.

Key words. ISM: abundances - ISM: clouds - ISM: molecules - stars: formation - stars: protostars

1. Introduction

The outer Galaxy (OG), namely the portion of the Galactic disk beyond the solar circle, is located at galactocentric distances (R_{GC}) approximately between 9 and 24 kpc, and it shows chemical properties significantly different from those of the inner Galaxy. Several chemical galactocentric gradient studies have been conducted, mapping the differences in elemental composition between the inner and outer Milky Way (e.g., C, N, O, Fe), using various tracers (i.e., H II regions, classical Cepheids, young OB stars, and planetary nebulae, among others). These works, focused on observational trends (e.g., Luck 2018; Bra-

gança et al. 2019; Méndez-Delgado et al. 2022) and chemodynamical studies (Jacobson et al. 2016; Stanghellini & Haywood 2018; Palla et al. 2020; Santos-Peral et al. 2021), indicate that the overall metallicity in the OG is lower than the solar one (e.g., a factor of four lower at $R_{GC} = 19$ kpc; Shimonishi et al. 2021). The elemental abundances of carbon, oxygen, and nitrogen - the three most abundant elements in the Universe after hydrogen and helium - decrease as a function of R_{GC} (e.g., Esteban et al. 2017; Arellano-Córdova et al. 2020), similarly to other heavier elements, following the radial metallicity gradient. This observational result is linked to the traditional view of the OG as being poorer in molecules than the solar neighborhoods and the

inner Galaxy. Moreover, based on the aforementioned scarcity of elements crucial for the formation of complex molecules and (rocky) planets, chemical evolution models excluded most of the OG from the so-called Galactic habitable zone (GHZ); that is, the region in the Milky Way where the probability for the development of habitable planets is highest: the optimal region is predicted to be an annulus of the Galactic disk from ~ 7 kpc extended up to $R_{GC} \sim 9$ kpc, with maximum habitability at ~ 8 kpc (Spitoni et al. 2014, 2017). This led to the consideration of the OG not being suitable for the formation of planetary systems in which Earth-like planets could be born and might be capable of sustaining life (Prantzos 2008; Ramírez et al. 2010).

Recent observational results challenged this prediction. First, the occurrence of Earth-like planets does not seem to depend on metallicity (e.g., Maliuk & Budaj 2020; Mulders et al. 2018). Second, the low rate of disruptive events in the OG suggests that it might be more favorable than the inner Galaxy for preserving life on potentially habitable planets (e.g., Piran & Jimenez 2014; Vukotić et al. 2016). Third, the detection of several complex organic molecules (COMs; e.g., CH_3OH , CH_3CCH , CH_3OCHO , CH_3OCH_3) of prebiotic interest in low-metallicity environments, such as star-forming regions in the OG (Shimonishi et al. 2021; Bernal et al. 2021; Fontani et al. 2022, 2024; Koelmay & Ziurys 2025) and the Magellanic Clouds (Sewito et al. 2018, 2022; Shimonishi et al. 2023; Golshan et al. 2024). Overall, these results suggest that environments prone to the presence of molecular precursors of life and Earth-like planets might be widespread in the Milky Way, including the OG.

The project CHEMical complexity in the outer Galaxy (CHEMOUT; Fontani et al. 2022, 2022b, Colzi et al. 2022, Fontani et al. 2024), performed with the IRAM 30 m single-dish telescope, is aimed at deriving the molecular composition in 35 star-forming regions of the OG ($R_{GC} \sim 9 - 24$ kpc). The main results obtained in the previous works of the CHEMOUT project are (1) both the molecular detection rates and the molecular abundances of some organic species –namely HCO, H_2CO , and CH_3OH – do not vary significantly with R_{GC} (Fontani et al. 2022, 2022b); (2) the $^{14}\text{N}/^{15}\text{N}$ ratio as a function of R_{GC} is consistent with chemical-evolution models in which ^{15}N comes from novae (Colzi et al. 2022); (3) the high-angular-resolution maps of the target with the highest R_{GC} (WB89-670 at $R_{GC} \sim 23.4$ kpc) reveal chemical differentiation at core scales and, above all, a [C/H] abundance higher than expected at such a high galactocentric distance (Fontani et al. 2024).

The results obtained so far indicate a lack of decrease in the inspected molecular abundances, which, however, was limited to three species (HCO, H_2CO , and CH_3OH) and only 15 sources. In this paper, we analyze the molecules detected in more than 60% of the CHEMOUT sample according to Fontani et al. (2022), namely HCN, HCO^+ , $c\text{-C}_3\text{H}_2$, H^{13}CO^+ , HCO, and SO, and revise the molecular abundances of H_2CO and CH_3OH from Fontani et al. (2022b), using H_2 column densities from the new NIKA2 dust continuum maps. In Sect. 2, we describe the observational data used in this paper. In Sect. 3, we describe the methods implemented in the data analysis. The results are presented and discussed in Sect. 4 and 5. The conclusions and the outlooks are summarized in Sect. 6.

2. Observations

2.1. IRAM 30 m observations

This work is based on the observations done for the CHEMOUT project, described in Papers I and II (Fontani et al. 2022, 2022b),

performed with the Institut de RadioAstronomie Millimétrique (IRAM) 30 m telescope. The sample of sources analyzed in this paper is composed of the 35 star-forming regions, presented in Table 1 of Fontani et al. (2022). In some spectra, two velocity features are identified, and the sources listed in Table A.1 in this paper include both velocity components. In the analysis conducted, we used spectral windows at 3 and 2 mm, collected with the EMIR receiver and described in Table 1. The spectral windows of the project 004-18 (see Table 1) have been optimized to observe, at 3 mm, the $J = 1 - 0$ transitions of ^{13}C and ^{15}N isotopologues of HCN and HNC and, at 2 mm, the $J = 2 - 1$ line of DNC. The spectral windows observed in the project 042-21, at 3 and 2 mm, have been designed to observe several methanol and formaldehyde lines. For further details (e.g., pointing and focus, and weather conditions), we refer the reader to Fontani et al. (2022, 2022b).

2.2. NIKA2 bolometer observations

Millimeter continuum emission of 31 out of the 35 CHEMOUT targets was observed with the New IRAM KID Arrays 2 (NIKA2; Perotto et al. 2020) bolometer of the IRAM 30 m telescope in Pico Veleta, Spain. Observations were taken during the winter 2021 and 2023 pool seasons (February). The observations cover an almost circular region with a radius of ~ 9 arcmin, centered at the positions where the IRAM 30 m spectra have been observed (Table A.1). The dual-band capability of NIKA2 allowed us to simultaneously observe the dust’s thermal continuum emission at 2.0 and 1.2 mm (150 GHz and 260 GHz, respectively). The sensitivity achieved was ~ 1.5 mJy/beam at 1.2 mm and 0.5 mJy/beam at 2.0 mm. A more complete description of the observations and a detailed analysis of the maps will be presented in a forthcoming paper of the CHEMOUT series (Fontani et al. in prep). Here, we have used the maps only to derive the H_2 column densities (Sect. 3.2) to compute the molecular fractional abundances with respect to H_2 (Sect. 4.2).

Table 1: Observational set ups of CHEMOUT used in this paper.

Spectral windows (GHz)	Beam size (")	V_{res} (km s $^{-1}$)	B_{eff}	F_{eff}	T_{sys} (K)
85.310-87.130 ^a	28	~ 0.16	0.80	0.95	$\sim 120 - 200$
88.590-90.410 ^a	27	~ 0.16	0.80	0.95	$\sim 120 - 200$
90.400-98.180 ^b	25	~ 0.6	0.80	0.95	$\sim 100 - 150$
140.720-148.500 ^b	17	~ 0.4	0.73	0.93	$\sim 150 - 300$
148.470-150.290 ^a	15	~ 0.096	0.73	0.93	> 300
151.750-153.570 ^a	15	~ 0.096	0.73	0.93	> 300

Notes. The observational parameters presented include the frequency ranges observed (at 3 and 2 mm), velocity resolution (V_{res}) of the spectra, main beam efficiency (B_{eff}), forward efficiency (F_{eff}), and system temperature (T_{sys}).

^(a) Project 004-18 ^(b) Project 042-21

3. Analysis methods

3.1. Line fitting

The spectra were fit using the MADrid Data CUBe Analysis (MADCUBA¹; Martín et al. 2019) software. The transitions were identified using the Spectral Line Identification and LTE

¹ MADCUBA is a software developed at the Madrid Center of Astrobiology (CAB, CSIC-INTA) that enables the visualization and analy-

Modelling (SLIM) tool of MADCUBA, which makes use of the Jet Propulsion Laboratory (JPL; Pickett et al. 1998) and Cologne Database for Molecular Spectroscopy (CDMS; Müller et al. 2001) catalogs. The lines were fit using the AUTOFIT function of SLIM. This function produces the Gaussian synthetic spectrum that best matches the observed spectrum, assuming local thermodynamic equilibrium (LTE) conditions and the same fitting input parameters for all transitions of a given molecular species, which are total column density, N_{tot} ; excitation temperature, T_{ex} ; radial systemic velocity of the source, V_{LSR} ; full width at half-maximum of the line, FWHM; and angular size of the emission, θ_{S} .

For the source size, we assumed that the molecular emission fills the telescope beam, except for methanol and formaldehyde, where an estimation of the emission size was made in Fontani et al. (2022b) and updated in this paper as discussed in Sect. 4.1.1. Such an assumption is justified by the spatial extent of the emission of the dust (see Figs. B.1, B.2, B.3), as well as by the updated H_2CO and CH_3OH emission sizes shown in Table C.2. The excitation temperature, whenever an estimate was not possible through the fit, has been fixed to the one shown in Table A.1, which was estimated from the methanol lines for the 15 targets observed in Fontani et al. (2022b). For the remaining sources, we adopted an average T_{ex} of 10.7 K, derived from those sources for which methanol transitions were available. This approximation was necessary because it was not possible to estimate the temperature individually for each source based on the observed transitions. To evaluate the impact of this assumption, we computed N_{tot} in the range of excitation temperatures derived from methanol ($7 \leq T_{\text{ex}} \leq 15$ K; see Table A.1). In this T_{ex} range, the densities vary from the values shown in Tables C.1 and C.2 by a factor of two at most for the species studied (lowest for HCN, HCO^+ , and H^{13}CO^+ ; highest for SO).

As a detection criterion, we considered a line as detected if the signal-to-noise ratio (S/N) is greater than three (an estimation of the rms noise is given in Fontani et al. 2022), while the detection is considered as tentative for $2.5 \leq \text{S/N} \leq 3$. If a line is undetected (e.g., $\text{S/N} \leq 2.5$), MADCUBA provides a 3σ upper limit estimate to the line's integrated intensity from Eq. (29) of Martín et al. (2019). The upper limit on the integrated intensity is converted into a column-density upper limit using the SLIM parameters T_{ex} and θ_{S} . For these estimates, the average FWHM for each species across the sample was adopted (Sect. 5.2). This approach assumes that different molecules trace gases with different physical, kinematic, and excitation conditions.

The total column densities derived from transitions observed at frequencies corresponding to beam sizes different from $28''$ (i.e., the largest beam size among the IRAM 30 m telescope spectral windows) have been rescaled by a factor of $(\frac{\theta_{\text{beam}}}{28''})^2$. For H_2CO and CH_3OH , the column densities were estimated assuming a specific angular emission size (see Table C.2, and Sect. 4.1.1). In cases where the emission size exceeds $28''$, no correction was applied, under the assumption of uniform emission within the beam. Conversely, when the source size is smaller than $28''$, the same scaling factor was applied to account for beam dilution effects. The estimation of the molecular fractional abundances has been performed using

$$X_{\text{mol}} = \frac{N_{\text{tot}}}{N_{\text{H}_2}}, \quad (1)$$

sis of single spectra and data cubes: <https://cab.inta-csic.es/madcuba/>

where N_{tot} is the total molecular column density, and N_{H_2} is the H_2 column density (see Sect. 3.2).

3.2. Continuum analysis

For this paper, the analysis of these maps is limited to the extraction of the flux density from an angular region of $28''$ centered on the pointing centers of the molecular spectroscopic data. The dimension of the extracted region has been decided to match the larger beam size of IRAM 30 m in the studied spectral windows (Table 1). A complete description and a deeper analysis of the NIKA2 observations will be given in a forthcoming paper (Fontani et al. in prep.).

The column densities of H_2 , N_{H_2} were derived from the dust-continuum-emission maps. In the scales (and densities) traced by our observations, the thermal dust emission is expected to be optically thin. Under this assumption, we can use the following equation to derive N_{H_2} from the continuum flux density (e.g., Battersby et al. 2011):

$$N_{\text{H}_2} = \frac{\gamma F_{\nu}}{\Omega_{\text{S}} \kappa_{\nu} B_{\nu}(T_{\text{d}}) \mu_{\text{H}_2} m_{\text{H}}}, \quad (2)$$

where γ is the gas-to-dust ratio, F_{ν} is the continuum flux density at frequency ν , Ω_{S} is the source solid angle, κ_{ν} is the dust-mass opacity, T_{d} is the dust temperature, and μ_{H_2} is the mean molecular weight for molecular hydrogen that is assumed to be 2.8 (Kauffmann et al. 2008). The H_2 column density was estimated with both a constant gas-to-dust ratio ($\gamma = 100$) and a gas-to-dust ratio increasing with distance from the Galactic center from Giannetti et al. (2017) ($\gamma \sim 3000$ at $R_{\text{GC}} = 23.4$ kpc). T_{d} was derived under the assumption of thermal coupling between gas and dust, adopting the excitation temperatures obtained from the molecular line analysis of CH_3OH (Table A.1) or, for those sources where methanol is not detected, adopting 10.7 K (the average T_{ex} from CH_3OH). The dust-mass opacity was derived at the observed frequencies from the relation $\kappa_{\nu}/\kappa_{\nu_0} = (\nu/\nu_0)^{\beta}$, assuming $\kappa_{\nu_0} = 0.899$ at $\nu_0 = 230$ GHz (Ossenkopf & Henning 1994). The spectral index, β , was estimated, for each source, from the ratio between the flux densities at the two frequencies observed (150 and 260 GHz) with NIKA2 (Appendix B).

4. Results

4.1. Detection summary

A comprehensive molecular identification was performed over the whole sample to identify the species detected in the greatest number of targets. This allowed us to analyze abundance gradients as a function of galactocentric distance with the highest possible statistics. Over 30 molecular species have been detected, and the most frequently detected ones are HCN (39/39), HCO^+ (39/39), $c\text{-C}_3\text{H}_2$ (38/39), H^{13}CO^+ (30/39), HCO (29/39), and SO (25/39). The detection statistics over these species are already listed in Fontani et al. (2022). We also included H_2CO (18/18) and CH_3OH (17/18) among the species considered. The analysis of the HCO, H_2CO , and CH_3OH gradients was conducted by Fontani et al. (2022b); however, here, we present updated trends based both on the revised fits performed with MADCUBA (Sect. 4.1.1) and on our new H_2 column-density estimates from NIKA2 observations. The spectroscopic parameters of the transitions detected in these molecules are displayed in Table 3. In Appendix C, the best-fit parameters obtained from the analysis with MADCUBA, and the spectra of the fit transitions for HCN,

H^{13}CO^+ , and SO are shown in detail. The spectra of $c\text{-C}_3\text{H}_2$ and HCO^+ are shown in Fontani et al. (2022), and the ones of HCO , H_2CO , and CH_3OH in Fontani et al. (2022b). The results regarding the molecular column densities (e.g., their galactocentric gradients) are provided in Appendix D.

In Table A.1, the N_{H_2} values calculated assuming a gas-to-dust ratio from Giannetti et al. (2017) are presented. These values are used hereafter for the analysis. All the data, results, and discussions concerning fractional abundances with respect to H_2 are based on these estimates, rather than on those obtained assuming a fixed $\gamma = 100$. The NIKA2 dust continuum maps and the galactocentric gradients for H_2 column densities are shown in Appendix B.

Six sources (19383+2711, 19571+3113, WB89-006, WB89-060, WB89-080, and WB89-380) show multiple velocity features also reported in Fontani et al. (2022). Four of them (19383+2711, 19571+3113, WB89-006, and WB89-380) exhibit double-peak emission in most of the observed lines. Because the peak velocities of these two features are consistent in the different transitions in which they are detected, they probably arise from two clumps within the telescope beam that have an angular separation smaller than the beam itself. This is confirmed by the NIKA2 maps (Figs. B.1 - B.3), for 19383+2711 and 19571+3113, showing two different emission components in the beam of the IRAM 30 m telescope. WB89-006 and WB89-380 do not show a clear double peak in the continuum maps, but the two clumps could be non-resolved with NIKA2 or aligned along the line of sight. In principle, each of these clumps may have distinct physical and chemical properties and will therefore be analyzed separately in the following sections. For these, the peak velocities were estimated using the V_{LSR} of the $c\text{-C}_3\text{H}_2$ $J_{K_a, K_c} = 2_{1,2} - 1_{0,1}$ line, and we assumed the same Galactic longitude, ℓ , for both clumps, to estimate their galactocentric radius, R_{GC} , and heliocentric distance, d . The remaining two sources (WB89-060 and WB89-080) are characterized by a double peak, but only in some more intense and potentially optically thick lines (e.g., HCN and HCO^+) and do not show coherence in the peak velocities. Consequently, in these cases, the double-peaked line shapes are more likely due to high-optical-depth effects, such as (self-)absorption, rather than multiple velocity features. These have thus been analyzed as single sources, and the absorbed lines discarded from the analysis. Moreover, some transitions showed non-Gaussian, high-velocity wings. We decided to limit our analysis to the narrower component of the molecular emissions related to the line emission around the intensity peak, and thus arising from the bulk emission of the cores.

Table 2: Observed ranges of column densities, fractional abundances, and line widths of the studied species.

Species	N_{tot} (cm^{-2})	X_{mol}	FWHM (km s^{-1})
HCN	$(0.33 - 24) \times 10^{12}$	$(0.84 - 17) \times 10^{-11}$	0.6 - 3.8
HCO^+	$(0.31 - 8.8) \times 10^{12}$	$(0.34 - 6.8) \times 10^{-11}$	0.9 - 4.3
$c\text{-C}_3\text{H}_2$	$(0.31 - 3.5) \times 10^{12}$	$(0.34 - 10) \times 10^{-11}$	0.7 - 4.7
H^{13}CO^+	$(0.31 - 4.8) \times 10^{11}$	$(0.43 - 10) \times 10^{-12}$	0.6 - 4.9
HCO	$(0.58 - 7.6) \times 10^{12}$	$(0.57 - 23) \times 10^{-11}$	0.7 - 4.8
SO	$(0.24 - 5.2) \times 10^{13}$	$(0.21 - 5.2) \times 10^{-10}$	0.6 - 4.1
H_2CO	$(0.15 - 6.5) \times 10^{13}$	$(0.26 - 3.7) \times 10^{-10}$	1.6 - 4.0
CH_3OH	$(0.24 - 11) \times 10^{13}$	$(0.15 - 5.6) \times 10^{-10}$	1.0 - 4.0

4.1.1. Formaldehyde and methanol updated fits

The fits for H_2CO and CH_3OH have been revised due to an incorrect assumption in Fontani et al. (2022b), which originated from a conversion between T_{A}^* and T_{MB} . Since the beam efficiency η_{eff} of the telescope was not explicitly specified in Bernal et al. (2021), the values were taken from Appendix C.3 of the ARO 12m user manual; however, outdated efficiencies were inadvertently used. Updated efficiencies² have now been adopted to estimate the T_{MB} of these two species. For H_2CO at 2 mm we divided T_{A}^* by 0.81, and for CH_3OH at 3 mm we divided by 0.91. The source sizes for H_2CO and CH_3OH were re-estimated using Eq. 3 in Fontani et al. (2002). Consequently, the MADCUBA fits were recalculated, and the resulting parameters are reported in Appendix C. The excitation temperatures of CH_3OH are listed in Table A.1.

4.2. Fractional abundances

The molecular fractional abundances, X_{mol} , with respect to H_2 were computed through Eq. 1, with the molecular column densities from Tables C.1 and C.2, and the N_{H_2} from Table A.1. The values of X_{mol} are in ranges presented in Table 2. All the values are shown in Table 4. These values are estimated for 31 star-forming regions of the sample, i.e., the ones observed in the dust emission, for which we have the H_2 column densities. For sources exhibiting a double clump structure (see Sect. 4.1), the fractional abundances were obtained by summing the molecular column densities of the two components, and the galactocentric distances were determined as the average R_{GC} of the individual clumps.

The plots showing X_{mol} against R_{GC} for each molecule are shown in Fig. 1. For comparison, the fractional abundances calculated using a gas-to-dust ratio $\gamma = 100$ are also shown. A linear fit is performed for each plot, and the Pearson correlation coefficient³, ρ , is calculated to inspect possible (anti-)correlations. The linear fit applied to the data of fractional abundances, calculated using a gas-to-dust ratio from Giannetti et al. (2017), gives:

$$[\text{HCN}] = (-0.105 \pm 0.013) \text{ dex kpc}^{-1} \cdot R_{\text{GC}} - (8.79 \pm 0.20) \text{ dex}, \quad (3)$$

$$[\text{HCO}^+] = (-0.078 \pm 0.018) \text{ dex kpc}^{-1} \cdot R_{\text{GC}} - (9.50 \pm 0.28) \text{ dex}, \quad (4)$$

$$[c\text{-C}_3\text{H}_2] = (-0.058 \pm 0.021) \text{ dex kpc}^{-1} \cdot R_{\text{GC}} - (9.95 \pm 0.32) \text{ dex}, \quad (5)$$

$$[\text{H}^{13}\text{CO}^+] = (-0.039 \pm 0.025) \text{ dex kpc}^{-1} \cdot R_{\text{GC}} - (11.32 \pm 0.38) \text{ dex}, \quad (6)$$

$$[\text{HCO}] = (-0.057 \pm 0.026) \text{ dex kpc}^{-1} \cdot R_{\text{GC}} - (9.83 \pm 0.41) \text{ dex}, \quad (7)$$

$$[\text{SO}] = (-0.080 \pm 0.023) \text{ dex kpc}^{-1} \cdot R_{\text{GC}} - (8.98 \pm 0.36) \text{ dex}, \quad (8)$$

$$[\text{H}_2\text{CO}] = (-0.103 \pm 0.050) \text{ dex kpc}^{-1} \cdot R_{\text{GC}} - (8.42 \pm 0.75) \text{ dex}, \quad (9)$$

$$[\text{CH}_3\text{OH}] = (-0.146 \pm 0.054) \text{ dex kpc}^{-1} \cdot R_{\text{GC}} - (7.67 \pm 0.82) \text{ dex}. \quad (10)$$

4.3. Line widths

From the fit of the lines, we also obtained the full widths at half maximum (FWHMs). The measured FWHMs for the molecules studied are in the ranges shown in Table 2. The mean values of line width estimated for each molecule have been used in the

² From <https://aro.as.arizona.edu/?q=beam-efficiencies>.

³ This coefficient measures the strength and direction of the linear relationship between two variables, X and Y, and it is calculated as the covariance of X and Y divided by the product of their standard deviations. It ranges from -1 to $+1$, where $+1$ indicates perfect positive correlation, 0 indicates no linear correlation, and -1 indicates perfect negative correlation.

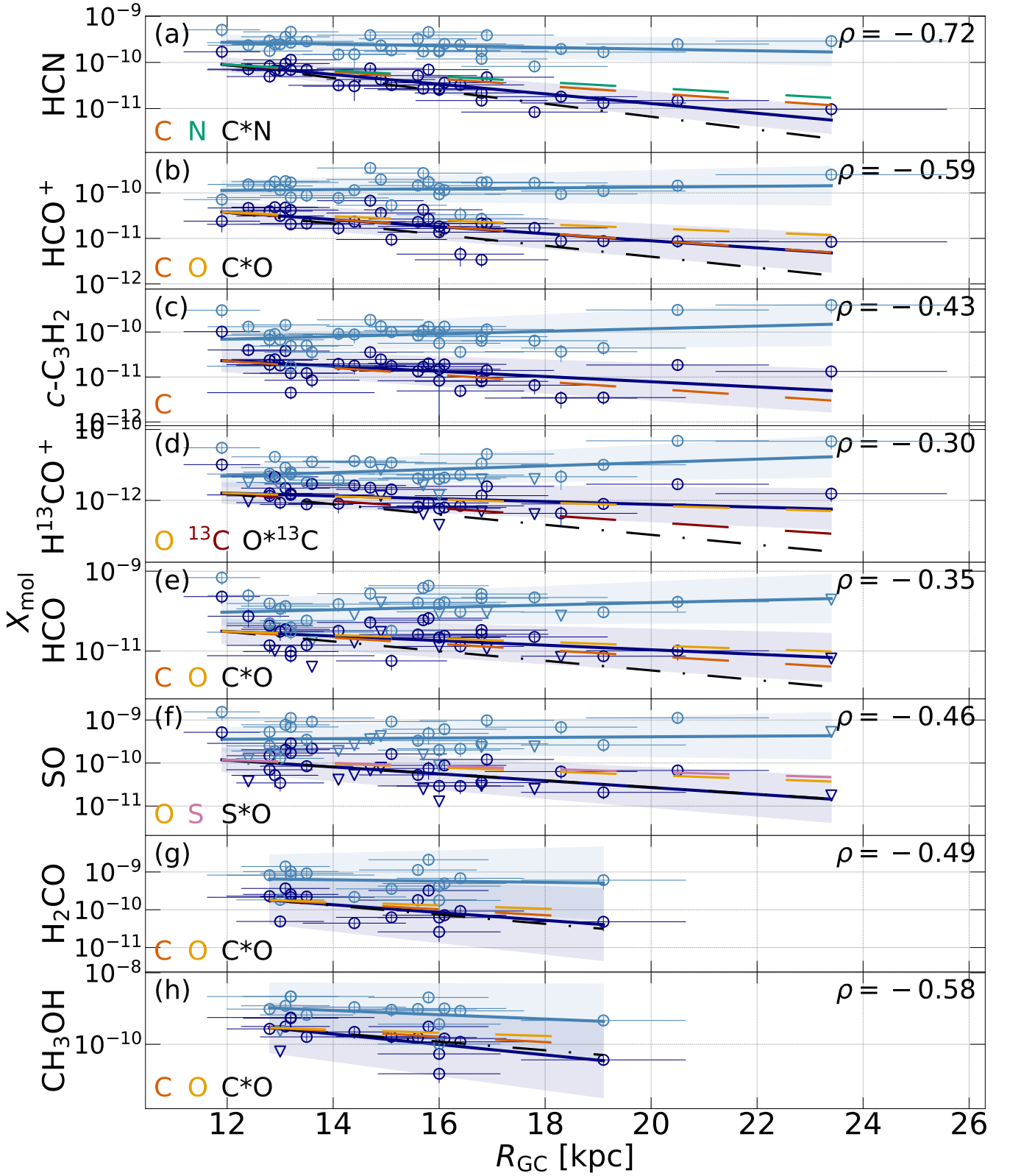


Fig. 1: Galactocentric gradients of fractional abundances with respect to H_2 , X_{mol} . The plot shows the trends for HCN (a), HCO^+ (b), $c\text{-C}_3\text{H}_2$ (c), H^{13}CO^+ (d), HCO (e), SO (f), H_2CO (g), and CH_3OH (h) as a function of the galactocentric radius (R_{GC}). The light blue data represent the abundances calculated using a constant gas-to-dust ratio ($\gamma = 100$), while the dark blue data illustrate those estimated using a non-constant gas-to-dust ratio ($\gamma = \gamma(R_{\text{GC}})$ from Giannetti et al. 2017). For both datasets, the linear regression results are shown as the light blue and dark blue lines, respectively. The 1σ error bars over the slope of the gradients are displayed for each fit. The upper-limit values are represented by triangles. The gradients of the elemental abundances of carbon (C and ^{13}C), nitrogen (N), oxygen (O), and sulfur (S), as reported by Méndez-Delgado et al. (2022), are plotted as dashed lines. The product of the parent elements of the species is represented, in each subplot, by a dash-dotted black line. All elemental trends are plotted with a vertical offset to align with the starting point of the molecular gradients derived using $\gamma(R_{\text{GC}})$, to facilitate comparison of their slopes with the linear fit of the molecular abundances. In the upper-right side of each subplot, the Pearson correlation coefficient, ρ , is shown (estimated only for the abundances estimated using the non-constant gas-to-dust ratio).

Table 3: Rest frequencies and other spectroscopic parameters of the studied and detected molecular transitions.

Molecule	Rest frequency (GHz)	Quantum numbers	E_u (K)	$\log(A_{ij}/s)$
HCN	88.63042	$J = 1 - 0, F = 1 - 1$	4.3	-4.6184
	88.63185	$J = 1 - 0, F = 2 - 1$	4.3	-4.6185
	88.63394	$J = 1 - 0, F = 0 - 1$	4.3	-4.6184
HCO ⁺	89.18852	$J = 1 - 0$	4.3	-4.3781
<i>c</i> -C ₃ H ₂	85.33889	$J_{K_a, K_c} = 2_{1,2} - 1_{0,1}$	6.4	-4.6341
	145.08959	$J_{K_a, K_c} = 3_{1,2} - 2_{2,1}$	16.0	-4.1696
H ¹³ CO ⁺	86.75429	$J = 1 - 0$	4.2	-4.4142
HCO	86.67076	$N_{K_a, K_c} = 1_{0,1} - 0_{0,0}, J = 3/2 - 1/2, F = 2 - 1$	4.2	-5.3289
	86.70836	$N_{K_a, K_c} = 1_{0,1} - 0_{0,0}, J = 3/2 - 1/2, F = 1 - 0$	4.2	-5.3377
	86.77746	$N_{K_a, K_c} = 1_{0,1} - 0_{0,0}, J = 1/2 - 1/2, F = 1 - 1$	4.2	-5.3366
	86.80578	$N_{K_a, K_c} = 1_{0,1} - 0_{0,0}, J = 1/2 - 1/2, F = 0 - 1$	4.2	-5.3268
SO	86.09395	$N = 2 - 1, J = 2 - 1$	19.3	-5.2799
H ₂ CO	140.839502	$J_{K_a, K_c} = 2_{1,2} - 1_{1,1}$	21.9	-4.2754
H ₂ CO	145.602949	$J_{K_a, K_c} = 2_{0,2} - 1_{0,1}$	10.5	-4.1072
CH ₃ OH	95.91431	$2(1, 2) - 1(1, 1) A^+$	21.4	-5.6031
CH ₃ OH	96.739358	$2(1, 2) - 1(1, 1) E_2$	12.5	-5.5923
CH ₃ OH	96.741371	$2(0, 2) - 1(0, 1) A^+$	7.0	-5.4675
CH ₃ OH	96.744545	$2(0, 2) - 1(0, 1) E_1$	20.1	-5.4676
CH ₃ OH	96.755501	$2(1, 1) - 1(1, 0) E_1$	28.0	-5.5810
CH ₃ OH	97.582798	$2(1, 1) - 1(1, 0) A^-$	21.6	-5.5806
CH ₃ OH	143.865795	$3(1, 3) - 2(1, 2) A^+$	28.3	-4.9712
CH ₃ OH	145.093707	$3(0, 3) - 2(0, 2) E_1$	27.1	-4.9096
CH ₃ OH	145.097370	$3(1, 3) - 2(1, 2) E_2$	19.5	-4.9602
CH ₃ OH	145.103152	$3(0, 3) - 2(0, 2) A^+$	13.9	-4.9093
CH ₃ OH	145.126191	$3(2, 2) - 2(2, 1) E_1$	36.2	-5.1693
CH ₃ OH	145.126386	$3(2, 1) - 2(2, 0) E_2$	39.8	-5.1638
CH ₃ OH	145.131855	$3(1, 2) - 2(1, 1) E_1$	35.0	-4.9490
CH ₃ OH	146.368328	$3(1, 2) - 2(1, 1) A^+$	28.6	-4.9488

estimation of the upper limits of the column densities, as an educated guess ($2.1 \pm 0.6 \text{ km s}^{-1}$ for HCN; $1.8 \pm 0.9 \text{ km s}^{-1}$ for HCO⁺; $2.1 \pm 1.0 \text{ km s}^{-1}$ for *c*-C₃H₂; $2.1 \pm 1.0 \text{ km s}^{-1}$ for H¹³CO⁺; $2.2 \pm 1.0 \text{ km s}^{-1}$ for HCO; $2.0 \pm 0.8 \text{ km s}^{-1}$ for SO; $2.3 \pm 0.7 \text{ km s}^{-1}$ for H₂CO; $1.9 \pm 0.8 \text{ km s}^{-1}$ for CH₃OH).

The plots of FWHM of HCN, HCO⁺, *c*-C₃H₂, H¹³CO⁺, HCO, SO, H₂CO, and CH₃OH as a function of the galactocentric distance are shown in Fig. 2. A linear fit is performed, and the Pearson correlation coefficient, ρ , is estimated. We find that, for all species, the line width shows an overall negative trend with R_{GC} , along with a weak negative correlation ($\rho \lesssim -0.2$).

5. Discussion

5.1. Galactocentric gradients of fractional abundances

The trends obtained for the molecular abundance (with respect to H₂) were compared with the galactocentric abundance gradients of carbon (both ¹²C and ¹³C), oxygen, nitrogen, and sulfur. These are constituting elements of the studied species, and the gradients were determined in Méndez-Delgado et al. (2022) through the analysis of the spectra of Galactic HII regions. The galactocentric gradient of ¹³C was estimated by coupling the carbon gradient with the galactocentric trend of the ¹³C/¹²C ratio from Yan et al. (2023). Among 8.34 kpc, the galactocentric distance

of the Sun, and 24 kpc, which is the distance of the most distant source in our sample, the abundance ratios [C/H], [¹³C/H], [N/H], [O/H], and [S/H] decrease by factors of approximately ~ 16 , ~ 36 , ~ 10 , ~ 5 , and ~ 4 , respectively. Extrapolating the gradients derived in the OG (Eqs. 3–8) to the Solar circle, over the same range of R_{GC} , we find that the abundance of the studied species, i.e., HCN, HCO⁺, *c*-C₃H₂, H¹³CO⁺, HCO, SO, H₂CO, and CH₃OH decrease by a factor of ~ 44 , ~ 17 , ~ 8 , ~ 4 , ~ 8 , ~ 18 , ~ 41 , and ~ 194 .

The decreasing rates of HCN, HCO⁺, *c*-C₃H₂, HCO, H₂CO, and CH₃OH are consistent, within the error bars, with that of [C/H]. This implies that, considering the dispersion and uncertainties in estimating these quantities, the fractional abundances of these carbon-bearing species scale with the elemental abundance of carbon ([C/H]) between 8.34 kpc and 24 kpc. This suggests that the efficiency in forming these molecules, which scales with the availability of the parent element, C, is at least as high as in the local Galaxy.

In contrast, the decreasing rate of SO appears steeper than that of [S/H]. For SO, the higher decreasing rate with respect to [S/H] indicates a lower efficiency of the formation of these molecules in the OG with respect to the local Galaxy. We speculate that a steeper decreasing trend for SO, which is the best shock tracer among those that we analyzed in this work, could indicate that, in the OG, outflows have a reduced influence on the

Table 4: Fractional abundance, X_{mol} , with respect to H_2 of HCN, HCO^+ , $c\text{-C}_3\text{H}_2$, H^{13}CO^+ , HCO, SO, H_2CO , and CH_3OH .

Source	X(HCN) $\times 10^{-11}$	X(HCO^+) $\times 10^{-11}$	X($c\text{-C}_3\text{H}_2$) $\times 10^{-11}$	X(H^{13}CO^+) $\times 10^{-12}$	X(HCO) $\times 10^{-11}$	X(SO) $\times 10^{-10}$	X(H_2CO) $\times 10^{-10}$	X(CH_3OH) $\times 10^{-10}$
19383+2711 ^a	6.7 (1.5)	3.1 (0.7)	1.8 (0.4)	0.9 (0.3)	3.1 (1.3)	0.36 (0.13)	0.49 (0.15)	≤ 0.6
19423+2541	7.0 (1.7)	2.1 (0.6)	1.2 (0.3)	0.7 (0.2)	1.4 (0.4)	0.8 (0.2)	2.2 (0.7)	1.6 (0.4)
19489+3030	6.7 (1.5)	4.9 (1.0)	2.5 (0.6)	4.6 (0.12)	≤ 1.0	0.5 (0.3)
19571+3113 ^a	7 (2)	4.7 (1.1)	4.0 (1.1)	≤ 0.9	7 (4)	≤ 0.4
20243+3853	8.3 (1.7)	4.0 (0.9)	2.4 (0.5)	1.3 (0.4)	4.3 (1.0)	0.7 (0.2)
WB89-002 ^b
WB89-006 ^a	3.1 (1.6)	2.3 (0.6)	1.8 (0.7)	2.6 (0.9)	≤ 1.6	≤ 0.5	0.44 (0.13)	2.2 (0.8)
WB89-014	4.3 (1.1)	3.6 (0.9)	2.5 (0.8)	≤ 1.3	≤ 3	≤ 0.8
WB89-031	3.2 (0.7)	1.7 (0.5)	2.0 (0.6)	0.8 (0.4)	3.2 (1.2)	≤ 0.4
WB89-035	9 (2)	4.8 (1.2)	3.8 (1.1)	2.2 (0.7)	3.5 (1.3)	2.0 (0.6)	3.7 (1.1)	3.2 (1.0)
WB89-040	17 (5)	2.4 (1.0)	10 (3)	10.2 (0.4)	23 (8)	5 (2)
WB89-060	0.8 (0.3)	2.9 (0.7)	≤ 0.4	2.2 (0.6)
WB89-076	3.2 (0.8)	0.9 (0.3)	1.8 (0.4)	2.0 (0.5)	0.6 (0.2)	1.6 (0.4)	0.63 (0.17)	1.6 (0.6)
WB89-080	4.9 (1.1)	...	1.9 (0.7)	1.6 (0.6)	1.4 (0.5)	1.5 (0.4)	2.3 (0.7)	2.7 (0.8)
WB89-083	7.4 (1.5)	6.8 (1.4)	3.6 (0.8)	2.3 (0.6)	5.2 (1.8)	≤ 0.7
WB89-152 ^b
WB89-283	7.0 (1.8)	2.7 (0.7)	2.0 (0.7)	0.8 (0.3)	7 (2)	0.8 (0.3)	3.2 (1.0)	3.1 (0.8)
WB89-288	1.5 (0.3)	2.1 (0.4)	1.0 (0.3)	≤ 0.5	3.4 (1.0)	≤ 0.3
WB89-315 ^b
WB89-379	3.3 (0.8)	0.5 (0.2)	0.49 (0.14)	0.7 (0.2)	1.3 (0.4)	0.3 (0.11)	0.9 (0.2)	1.2 (0.4)
WB89-380 ^a	2.6 (0.7)	1.4 (0.4)	0.8 (0.8)	0.6 (0.2)	≤ 1.3	0.29 (0.10)	0.26 (0.12)	0.54 (0.17)
WB89-391	3.6 (0.9)	1.7 (0.4)	1.9 (0.5)	0.63 (0.19)	2.4 (0.6)	0.9 (0.2)	0.7 (0.2)	1.5 (0.4)
WB89-399	2.7 (0.6)	1.8 (0.4)	1.5 (0.3)	≤ 0.2	2.2 (0.6)	≤ 0.13	0.6 (0.2)	0.15 (0.07)
WB89-437	11 (3)	4.2 (0.9)	1.2 (0.3)	1.6 (0.4)	1.0 (0.3)	1.7 (0.4)	2.6 (0.7)	5.4 (1.3)
WB89-440	2.7 (0.5)	4.3 (0.8)	1.7 (0.4)	≤ 0.4	5.9 (1.4)	≤ 0.2
WB89-501	5.2 (1.2)	2.3 (0.6)	1.3 (0.3)	0.7 (0.2)	2.6 (0.7)	0.53 (0.14)	1.8 (0.5)	1.6 (0.5)
WB89-529	0.84 (0.19)	1.7 (0.3)	0.7 (0.2)	≤ 0.4	2.3 (0.6)	≤ 0.2
WB89-572	1.8 (0.4)	0.9 (0.2)	0.34 (0.14)	0.4 (0.2)	≤ 0.7	0.6 (0.2)
WB89-621	6.9 (1.7)	2.0 (0.5)	0.49 (0.13)	1.4 (0.4)	0.8 (0.3)	2.9 (0.7)	2.1 (0.6)	5.6 (1.5)
WB89-640	2.2 (0.4)	0.34 (0.11)	0.80 (0.19)	1.4 (0.3)	2.6 (0.6)	0.35 (0.11)
WB89-670	1.0 (0.3)	0.8 (0.2)	1.3 (0.5)	1.6 (0.6)	≤ 0.6	≤ 0.18
WB89-705	1.5 (0.4)	0.9 (0.2)	1.9 (0.5)	2.9 (0.8)	1.0 (0.4)	0.67 (0.18)
WB89-789	1.3 (0.3)	0.87 (0.19)	0.35 (0.11)	0.8 (0.2)	0.7 (0.2)	0.21 (0.07)	0.5 (0.2)	0.37 (0.11)
WB89-793	4.8 (1.2)	2.1 (0.5)	1.4 (0.5)	2.5 (0.7)	≤ 1.1	1.2 (0.4)
WB89-898 ^b

Notes. ^(a) Sources characterized by a double clump. The fractional abundances have been estimated by summing the total column densities over both clumps. ^(b) Sources lacking NIKA2 observations, for which no H_2 column density could be estimated.

gas composition compared to the local Galaxy. This result would be consistent with the decreasing line width with R_{GC} (Sect. 4.3). Another shock tracer is CH_3OH , which, although its decreasing trend is marginally consistent with that of carbon, exhibits the most pronounced reduction among the species investigated in the OG. The steep decreasing trend of CH_3OH could also arise from a less efficient grain-surface chemistry in the OG. The results concerning HCO, H_2CO , and CH_3OH , obtained with the updated abundances (and distances), confirm the ones of Fontani et al. (2022b). In Fontani et al. (2024), a correlation between the abundances of CH_3OH and SO was found, which is confirmed over the entire CHEMOUT sample, although no correlation between the line widths of these two species is observed, hinting that they are not tracing the same gas components.

The decreasing rate of H^{13}CO^+ , although lower than that of $^{13}\text{C}/\text{H}$, aligns well with the decreasing rate observed for oxygen. This correlation is not observed for HCO^+ , whose decreasing rate is consistent with carbon rather than oxygen. This dis-

crepancy could suggest a possible revision of the galactocentric gradient of the $^{13}\text{C}/^{12}\text{C}$ ratio, with a shallower trend at high R_{GC} , in agreement with the Galactic chemical evolution discussed in Colzi et al. (2022). Moreover, the detailed analysis of the $^{13}\text{C}/^{12}\text{C}$ ratios from the HCO^+ and H^{13}CO^+ lines will be the subject of a forthcoming paper (Colzi et al. in prep.). Therefore, the results regarding $c\text{-C}_3\text{H}_2$, HCO, and especially H^{13}CO^+ lead to the puzzling conclusion of observing more carbon-bearing molecules than the available carbon atoms in the OG, their decreasing rates being lower than that of $[\text{C}/\text{H}]$ (or $^{13}\text{C}/\text{H}$).

5.2. Galactocentric gradients of line widths

Considering the low temperature (Table A.1) of the sources, the thermal broadening of the emission lines can be neglected ($\sim 0.1 - 0.2 \text{ km s}^{-1}$); therefore, the line width is a good tracer of the gas turbulence of the sources. The decreasing galactocentric trends observed for the FWHM of the studied molecules suggest

that the sources tend to have lower turbulence as the distance from the Galactic center increases. Such a result would be in line with an environment becoming more and more quiescent at increasing R_{GC} . The nearest source to the Sun, WB89-002, is the only outlier that deviates from these trends.

This result is also consistent with the study of Lin et al. (2025), where the velocity dispersion of low- J ^{13}CO lines has been studied toward molecular clouds in the low-metallicity part of the Galactic disk. A decreasing trend of the line width is observed with R_{GC} , and the sub-virial dynamics observed in the metal-poor clouds hint at how the gas turbulence is not sufficient to counterbalance the cloud's self-gravity. As stated in Lin et al. (2025), in low-metallicity environments, the magnetic field may play a more dominant role, replacing gas turbulence in sustaining the clouds.

5.3. Galactocentric gradients of molecular ratios

Studies on the formation pathways of HCO^+ , H^{13}CO^+ (Klemperer 1970; Millar et al. 1991), HCO , H_2CO , and CH_3OH (Watanabe & Kouchi 2002; Fuchs et al. 2009; Minissale et al. 2016; Rivilla et al. 2019; Jiménez-Serra et al. 2025) have shown that their formation is linked to the presence of CO . In contrast, $c\text{-C}_3\text{H}_2$ is formed from "free" carbon (not bound in CO) (Thaddeus et al. 1985; Sipilä et al. 2016). Moreover, it is known that $[\text{C}/\text{O}]$ decreases with distance from the Galactic center (Méndez-Delgado et al. 2022). Therefore, we expect to have less free carbon in the OG to produce $c\text{-C}_3\text{H}_2$, because most of it would be locked in CO . This would lead to a prediction of an increasing trend for the $\text{CO}/c\text{-C}_3\text{H}_2$ ratio.

Considering the lack of direct CO measurements for our sample, we can use species containing C and O that are formed from CO , such as HCO^+ , H^{13}CO^+ , HCO , H_2CO , and CH_3OH . In Fig. 3, the galactocentric gradients of these ratios are presented. No clear trends arise from the data, which are also characterized by $|\rho| < 0.2$ (except for methanol, for which we have $\rho \sim -0.3$). The ratio between H^{13}CO^+ and $c\text{-C}_3\text{H}_2$ is the only one presenting a marginally increasing trend (in agreement with the formation pathways and the C/O abundance); however, it is too shallow to be considered reliable.

5.4. Caveats and uncertainties

The comparison between observations and chemical models by Fontani et al. (2024) for WB89-670 suggests that the methanol could be sub-thermally excited: the kinetic temperatures predicted by chemical modeling are in the $\sim 20 - 40$ K range, while the excitation temperatures are on the order of ~ 10 K. Therefore, an important caveat arises from the assumed T_{ex} for the species for which we cannot estimate it directly from the observations.

Furthermore, the sources are located in a range of heliocentric distances, d , between 3 and 15.1 kpc, which implies that the linear scale probed is not the same in all targets. Fontani et al. (2024) demonstrated the presence of a high differentiation at smaller angular scales in WB89-670, and hence the average column densities derived in this work refer to linear scales with (eventually) different average conditions. However, this caveat is typical of source surveys, and in any case, we compare emissions arising from core envelopes in all targets.

Some results may also be influenced by low statistics, particularly within certain R_{GC} ranges, where the data characterizing a few sources have a bigger impact on the gradients. This con-

cern is more significant for formaldehyde and methanol, given their even lower sampling rates (only 18 molecular clumps of 39 are observed in H_2CO and CH_3OH spectral windows), over a smaller R_{GC} range (Fontani et al. 2022b).

Column densities of species such as HCN or HCO^+ might be affected by large optical-depth effects in the observed lines, which could impact the derived Galactocentric gradients. However, for HCN , the column densities were corrected by the line opacity (Table C.1) obtained from the hyperfine structure of the observed transition, and both HCN and HCO^+ were observed also in their less abundant ^{13}C -bearing isotopologues (see Appendix E for the gradient of H^{13}CN). Therefore, a gradient can also be inferred for these species using these isotopologues, expected to be optically thin.

Moreover, in the comparison between molecular and elemental trends, a further caveat comes from the fact that the elemental abundance gradients are extrapolated in the extreme OG ($R_{GC} \gtrsim 16$ kpc), where observations are sparse and thus the gradients are poorly constrained, and could be different from those at $R_{GC} \leq 16$ kpc. Indeed, recent studies have reported evidence of a flattening of the metallicity gradient at large galactocentric radii, which could influence the observed molecular abundances and potentially explain the unexpectedly high chemical complexity in the outskirts of the Galaxy (Donor et al. 2020; Myers et al. 2022; Magrini et al. 2023; Da Silva et al. 2023).

6. Conclusions and outlooks

In this work, we studied the chemical composition of 35 star-forming regions in the OG ($9 \leq R_{GC} \leq 24$ kpc), using IRAM 30 m telescope data from the CHEMOUT project. We identified 39 molecular clumps and analyzed the molecular species detected in the greatest number of targets across our sample; i.e., HCN (39/39), HCO^+ (39/39), $c\text{-C}_3\text{H}_2$ (38/39), H^{13}CO^+ (30/39), HCO (29/39), and SO (25/39). We estimated their column densities and calculated the fractional abundances of these species with respect to H_2 . We also updated the abundances of H_2CO (18/18) and CH_3OH (17/18) from Fontani et al. (2022b), using the H_2 column densities obtained from the new NIKA2 continuum maps.

The fractional abundances of the studied species with respect to H_2 estimated assuming a gas-to-dust ratio dependent on R_{GC} (Giannetti et al. 2017) show a decreasing trend with the galactocentric radius. For HCN , HCO^+ , $c\text{-C}_3\text{H}_2$, HCO , SO , H_2CO , and CH_3OH the abundances scale as the elemental abundance of carbon ($[\text{C}/\text{H}]$) between the solar circle and ~ 24 kpc. This indicates that the efficiency in the formation of these molecules, which scales with the availability of the parent element (i.e., C), is at least as high as that found in the local Galaxy. Instead, the decreasing rate of SO is higher than that of $[\text{S}/\text{H}]$, indicating a lower efficiency in the formation of this species in the OG. Conversely, the decreasing rate of H^{13}CO^+ presents the puzzling result that it is lower than that of $[\text{C}^{13}/\text{H}]$, resulting in a higher formation efficiency in the OG compared to the inner Galaxy.

The galactocentric gradients of the abundances indicate how the metallicity of the environment, which scales as effectively with R_{GC} , does not affect the formation efficiency of most of the molecules studied, even for so-called prebiotic molecules such as formaldehyde. Metallicity appears to act mostly as a scaling factor for the molecular abundances relative to the elemental ones. The role of metallicity in the efficiency of molecule formation may become evident when studying molecules more complex than methanol, and/or it could be hidden by other environmental factors such as the radiation field, gas

temperature, or cosmic ionization rate, which may counterbalance its effect. These results confirm (after the previous papers of the CHEMOUT series) that the presence of organic molecules and tracers of protostellar activity is ubiquitous in the low-metallicity environment of the OG.

The next step for the CHEMOUT project is to infer a more precise kinetic temperature of the sources to better estimate the column densities from the line analysis. Determining this parameter will also help to reduce the space parameters on a chemical modeling analysis (e.g., using UCLCHEM; Holdship et al. 2017), which is crucial to inferring the environmental differences of the star-forming regions in the different areas of the Galaxy and understanding the parameters driving the chemistry (Vermariën et al. 2025). The comparison between high-resolution observations and chemical models is crucial to disentangling the several contributions to these formation processes.

It is furthermore crucial to enhance the statistics acquired as much as we can. In fact, given the scarcity of star-forming regions in the extreme OG, the data we have for $R_{GC} \gtrsim 20$ kpc weigh significantly on the overall trends. Increasing the observed sample is essential to constraining the gradients obtained and securing more precise results over the ongoing chemistry in this region of the Milky Way.

Acknowledgements. We thank the anonymous referee for providing valuable comments and suggestions that improved the scientific content of this paper. F.F. is grateful to the IRAM 30 m staff for their precious help during the observations. L.C. and V.M.R. acknowledge support from grant no. PID2022-136814NB-I00 by the Spanish Ministry of Science, Innovation and Universities/State Agency of Research MICIU/AEI/10.13039/501100011033 and by ERDF, UE. V.M.R. also acknowledges support from the grant RYC2020-029387-I funded by MICIU/AEI/10.13039/501100011033 and by "ESF, Investing in your future", and from the Consejo Superior de Investigaciones Científicas (CSIC) and the Centro de Astrobiología (CAB) through the project 20225AT015 (Proyectos intramurales especiales del CSIC); and from the grant CNS2023-144464 funded by MICIU/AEI/10.13039/501100011033 and by "European Union NextGenerationEU/PRTR". The research leading to these results has received funding from the European Union's Horizon 2020 research and innovation programme under grant agreement nos. 730562 and 101004719 (ORP: <https://www.orp-h2020.eu>). SV and GV acknowledge support from the European Research Council (ERC) Advanced grant MOPPEX 833460. A.S.-M. acknowledges support from the RYC2021-032892-I grant funded by MCIN/AEI/10.13039/501100011033 and by the European Union "Next GenerationEU"/PRTR, as well as the program Unidad de Excelencia María de Maeztu CEX2020-001058-M, and support from the PID2023-146675NB-I00 (MCI-AEI-FEDER, UE).

References

Arellano-Córdova, K. Z., Esteban, C., García-Rojas, J., & Méndez-Delgado, J. E. 2020, *MNRAS*, 496, 1051
 Battersby, C., Bally, J., Ginsburg, A., et al. 2011, *A&A*, 535, A128
 Bernal, J., Sefhus, C., & Ziurys, L. 2021, *ApJ*, 922, 106
 Blair, S. K., Magnani, L., Brand, J., & Wouterloot, J. G. 2008, *AsBio*, 8, 59
 Bragança, G., Daflon, S., Lanz, T., et al. 2019, *A&A*, 625, A120
 Colzi, L., Romano, D., Fontani, F., et al. 2022, *A&A*, 667, A151
 Da Silva, R., d'Orazi, V., Palla, M., et al. 2023, *A&A*, 678, A195
 Donor, J., Frinchauboy, P. M., Cunha, K., et al. 2020, *AJ*, 159, 199
 Esteban, C., Fang, X., García-Rojas, J., & Toribio San Cipriano, L. 2017, *MNRAS*, 471, 987
 Fontani, F., Cesaroni, R., Caselli, P., & Olmi, L. 2002, *A&A*, 389, 603
 Fontani, F., Colzi, L., Bizzocchi, L., et al. 2022, *A&A*, 660, A76
 Fontani, F., Schmiedeke, A., Sánchez-Monge, A., et al. 2022b, *A&A*, 664, A154
 Fontani, F., Vermariën, G., Viti, S., et al. 2024, *A&A*, 691, A180
 Fuchs, G., Cuppen, H., Ioppolo, S., et al. 2009, *A&A*, 505, 629
 Giannetti, A., Leurini, S., König, C., et al. 2017, *A&A*, 606, L12
 Golshan, R. H., Sánchez-Monge, Á., Schilke, P., et al. 2024, *A&A*, 688, A3
 Hachisuka, K., Choi, Y., Reid, M., et al. 2015, *ApJ*, 800, 2
 Holdship, J., Viti, S., Jiménez-Serra, I., Makrymallis, A., & Priestley, F. 2017, *AJ*, 154, 38
 Jacobson, H. R., Friel, E., Jílková, L., et al. 2016, *A&A*, 591, A37

Jiménez-Serra, I., Megías, A., Salaris, J., et al. 2025, *A&A*, 695, A247
 Kauffmann, J., Bertoldi, F., Bourke, T. L., Evans, N. J., & Lee, C. W. 2008, *A&A*, 487, 993
 Klemperer, W. 1970, *Nature*, 227, 1230
 Koelmay, L., & Ziurys, L. 2025, *ApJ*, 986, 122
 Lin, L., Zhang, Z.-Y., Wang, J., et al. 2025, *Nat. Astron.*, 1
 Luck, R. E. 2018, *AJ*, 156, 171
 Magrini, L., Vázquez, C. V., Spina, L., et al. 2023, *A&A*, 669, A119
 Maliuk, A., & Budaj, J. 2020, *A&A*, 635, A191
 Martín, S., Martín-Pintado, J., Blanco-Sánchez, C., et al. 2019, *A&A*, 631, A159
 Méndez-Delgado, J., Amayo, A., Arellano-Córdova, K., et al. 2022, *MNRAS*, 510, 4436
 Millar, T., Bennett, A., Rawlings, J., Brown, P., & Charnley, S. 1991, *A&A*, 87, 585
 Minissale, M., Dulieu, F., Cazaux, S., & Hocuk, S. 2016, *A&A*, 585, A24
 Mulders, G. D., Pascucci, I., Apai, D., & Ciesla, F. J. 2018, *AJ*, 156, 24
 Müller, H. S., Thorwirth, S., Roth, D., & Winnewisser, G. 2001, *A&A*, 370, L49
 Myers, N., Donor, J., Spoo, T., et al. 2022, *AJ*, 164, 85
 Ossenkopf, V., & Henning, T. 1994, *A&A*, 291, 943
 Palla, M., Matteucci, F., Spitoni, E., Vincenzo, F., & Grisoni, V. 2020, *MNRAS*, 498, 1710
 Perotto, L., Ponthieu, N., Macías-Pérez, J., et al. 2020, *A&A*, 637, A71
 Pickett, H., Poynter, R., Cohen, E., et al. 1998, *J. Quant. Spectrosc. Radiat. Transf.*, 60, 883
 Piran, T., & Jimenez, R. 2014, *Phys. Rev. Lett.*, 113, 231102
 Prantzos, N. 2008, *Space Sci. Rev.*, 135, 313
 Ramírez, I., Asplund, M., Baumann, P., Melendez, J., & Bensby, T. 2010, *A&A*, 521, A33
 Rivilla, V., Beltrán, M., Vasyunin, A., et al. 2019, *MNRAS*, 483, 806
 Russeil, D., Zavagno, A., Mège, P., et al. 2017, *A&A*, 601, L5
 Santos-Peral, P., Recio-Blanco, A., Kordopatis, G., Fernández-Alvar, E., & de Laverny, P. 2021, *A&A*, 653, A85
 Sewilo, M., Cordiner, M., Charnley, S. B., et al. 2022, *ApJ*, 931, 102
 Sewilo, M., Indebetouw, R., Charnley, S. B., et al. 2018, *ApJL*, 853, L19
 Shimonishi, T., Izumi, N., Furuya, K., & Yasui, C. 2021, *ApJ*, 922, 206
 Shimonishi, T., Tanaka, K. E., Zhang, Y., & Furuya, K. 2023, *ApJL*, 946, L41
 Sipilä, O., Spezzano, S., & Caselli, P. 2016, *A&A*, 591, L1
 Spitoni, E., Giovannini, L., & Matteucci, F. 2017, *A&A*, 605, A38
 Spitoni, E., Matteucci, F., & Sozzetti, A. 2014, *MNRAS*, 440, 2588
 Stanghellini, L., & Haywood, M. 2018, *ApJ*, 862, 45
 Thaddeus, P., Vrtilik, J., & Gottlieb, C. 1985, *ApJ*, 299, L63
 Vermariën, G., Viti, S., Heyl, J., & Fontani, F. 2025, *A&A*, 699, A18
 Vukotić, B., Steinhauser, D., Martínez-Aviles, G., et al. 2016, *MNRAS*, 459, 3512
 Watanabe, N., & Kouchi, A. 2002, *ApJ*, 571, L173
 Yan, Y., Henkel, C., Kobayashi, C., et al. 2023, *A&A*, 670, A98

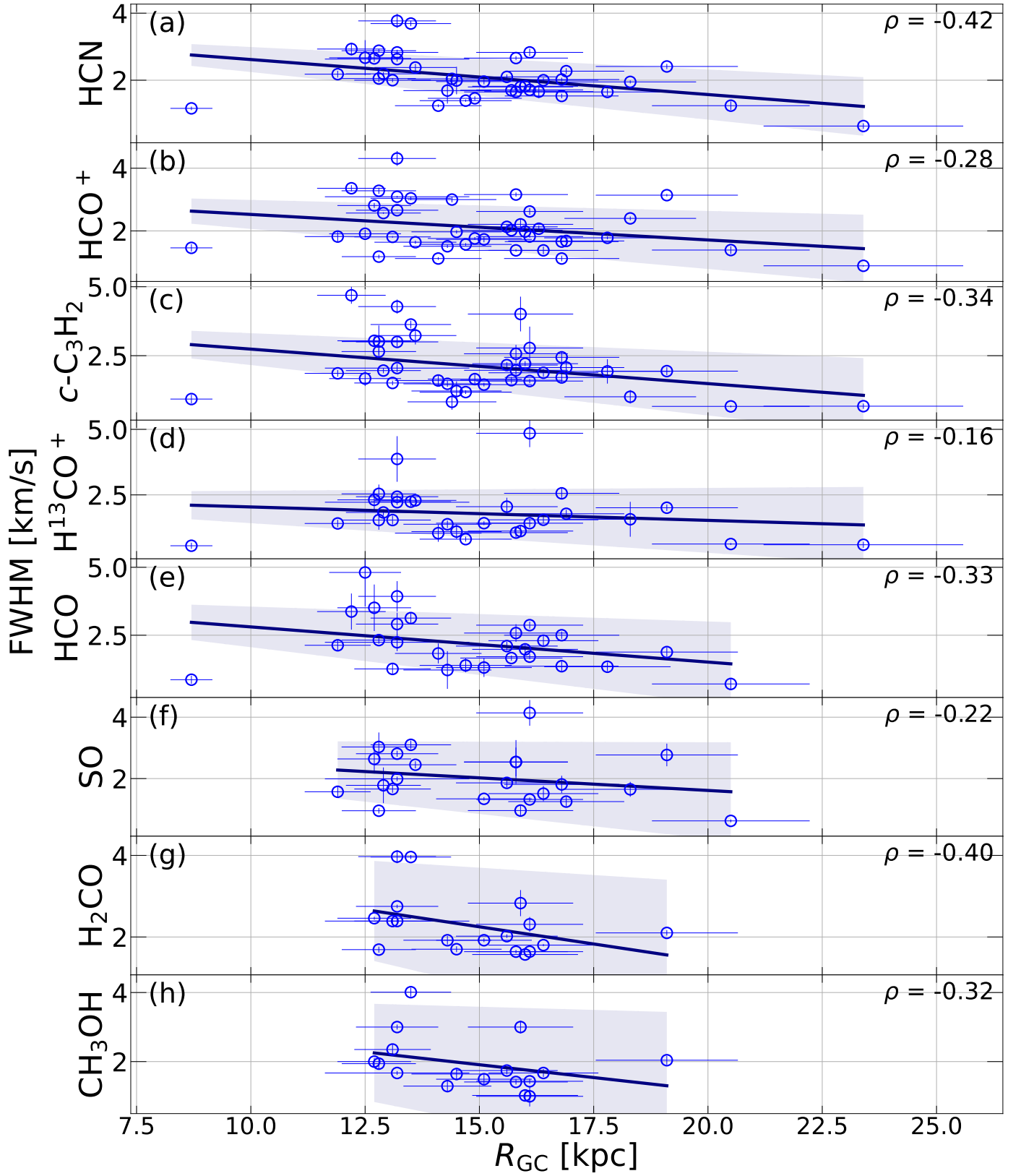


Fig. 2: Galactocentric gradients of line widths, FWHM. The plot shows the trends for HCN (a), HCO⁺(b), *c*-C₃H₂(c), H¹³CO⁺(d), HCO (e), SO (f), H₂CO (g), and CH₃OH (h) as a function of the galactocentric radius (R_{GC}). The linear fit results are shown as dark blue lines. The 1σ error bars over the slope of the gradients are displayed for each fit. In the upper right side of each subplot, the Pearson correlation coefficient, ρ , is shown.

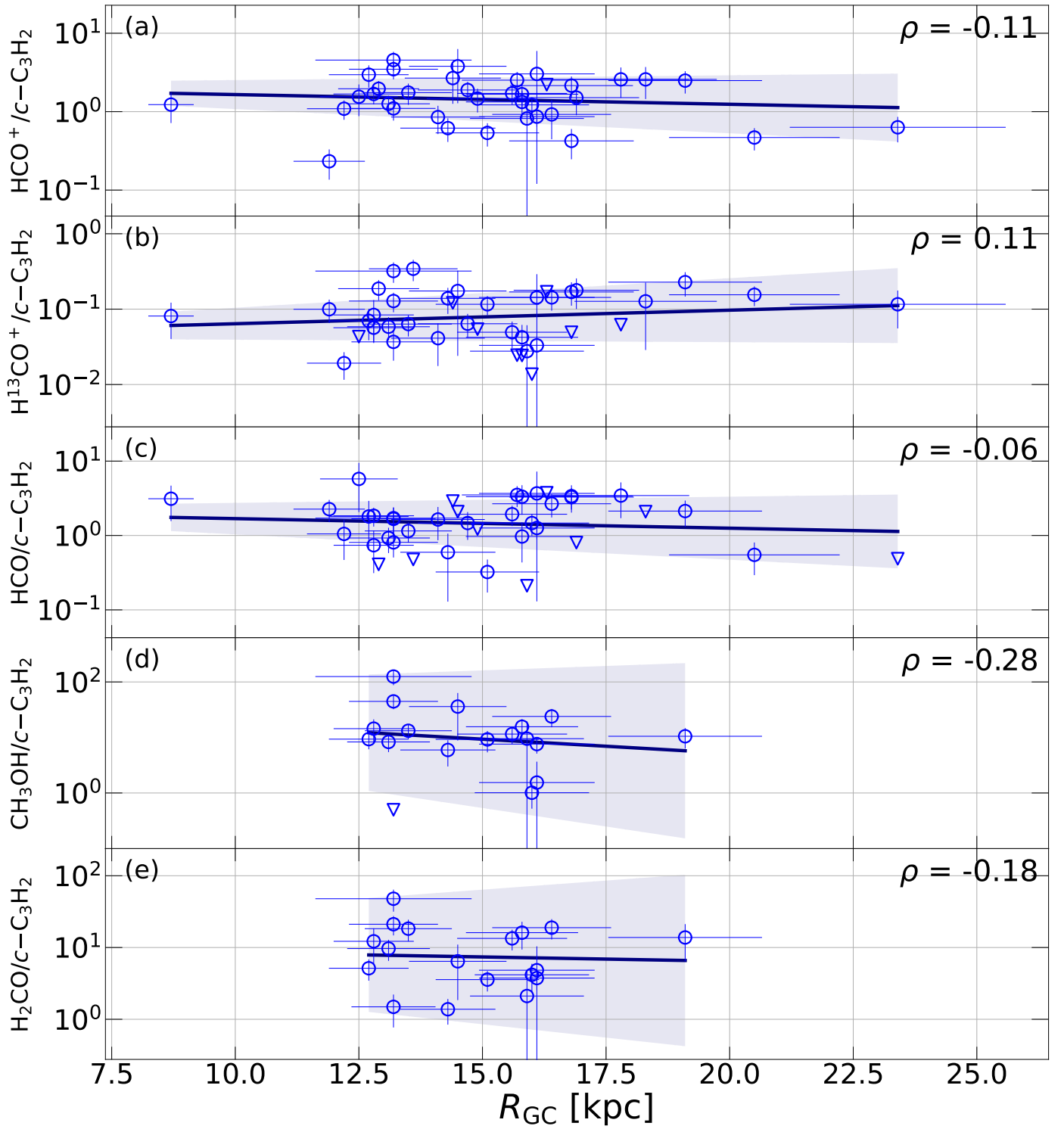


Fig. 3: Galactocentric gradients of molecular ratios. The plot shows the trend of the ratios between CO molecule products (i.e., HCO^+ , H^{13}CO^+ , HCO , CH_3OH , and H_2CO) and $c\text{-C}_3\text{H}_2$, as a function of galactocentric radius (R_{GC}). The 1σ error bars over the slope of the gradients are displayed for each molecular fit. The upper limit values are represented with triangles. The linear fit results are shown as the dark blue lines. The 1σ error bars over the slope of the gradients are displayed for each fit. In the upper right side of each subplot, the Pearson correlation coefficient, ρ , is shown.

Appendix A: The CHEMOUT sample

Table A.1 presents the observed sample together with its main properties.

Appendix B: Millimeter continuum maps and H₂ column densities

In this appendix, we show the millimeter continuum maps obtained with the IRAM 30m bolometer NIKA2 (Figs. B.1-B.4). We observed 31 out of the 35 CHEMOUT targets. A detailed analysis of the maps will be presented in a forthcoming paper (Fontani et al. in prep.).

In Table B.1, all the parameters derived from the continuum maps, and used to estimate the H₂ column densities, are presented. The fluxes have been extracted from the NIKA2 maps using a 28'' beam, matching the widest beam size of the spectral data centered at the same position from which we observed the IRAM 30m spectra. The spectral index β is estimated using the following equation:

$$\beta = \frac{\log\left(\frac{F_{\nu_2} B_{\nu_1}(T_d)}{F_{\nu_1} B_{\nu_2}(T_d)}\right)}{\log\frac{\nu_2}{\nu_1}}, \quad (\text{B.1})$$

where ν_2 and ν_1 , are 150 and 260 GHz (i.e., the frequencies corresponding to 2.0 and 1.2 mm), and T_d is the assumed dust temperature (see Sect. 3.2). In Fig. B.5, the galactocentric trends of H₂ are shown. The dataset estimated with a non-constant gas-to-dust ratio $\gamma = \gamma(R_{GC})$ (Giannetti et al. 2017) exhibits a positive trend with increasing values of R_{GC} , and a weak, positive correlation ($\rho = 0.19$), which is due to the increasing γ (Sect. 3.2).

Table B.1: Parameters (i.e., fluxes, gas-to-dust ratios γ , and spectral index β) used in the calculation of the H₂ column densities.

Source	γ	β	$F_{2.0\text{mm}}$ (mJy)	$F_{1.2\text{mm}}$ (mJy)
19383+2711	372	0.417	178 (5)	519 (17)
19423+2541	412	1.051	127 (10)	499 (38)
19489+3030	365	2.248	19 (1)	148 (7)
19571+3113	330	0.182	70 (2)	175 (9)
20243+3853	358	0.875	47 (2)	172 (7)
WB89-006	493	1.826	20 (1)	119 (6)
WB89-014	545	1.329	8.3 (0.4)	39 (3)
WB89-031	464	1.744	12.2 (0.5)	72 (3)
WB89-035	380	1.761	18 (1.6)	111 (9)
WB89-040	299	0.514	11 (1)	33 (4)
WB89-060	420	1.836	57 (4)	354 (28)
WB89-076	567	1.978	14.6 (0.7)	85 (4)
WB89-080	358	1.819	16.8 (0.6)	98 (3)
WB89-083	523	1.947	5.0 (0.2)	33 (1.0)
WB89-283	653	1.711	13.1 (0.7)	83 (5)
WB89-288	797	1.955	9.2 (0.2)	61 (1.6)
WB89-379	736	2.063	20 (1.5)	134 (9)
WB89-380	679	0.289	242 (18)	664 (42)
WB89-391	693	2.021	20 (1.6)	133 (8)
WB89-399	679	0.922	57 (2)	216 (10)
WB89-437	403	1.802	87 (5)	546 (34)
WB89-440	640	1.037	22 (1)	88 (3)
WB89-501	627	1.893	28 (1.6)	181 (10)
WB89-529	974	2.044	15.8 (0.5)	110 (3)
WB89-572	1077	1.928	15 (1)	98 (6)
WB89-621	388	1.872	63 (4)	394 (28)
WB89-640	797	1.808	53 (1.2)	324 (7)
WB89-670	2991	2.010	6.0 (0.4)	41 (3)
WB89-705	1673	1.026	8.3 (0.3)	33 (2)
WB89-789	1264	1.842	41 (2)	247 (13)
WB89-793	813	1.641	19 (1.0)	106 (6)

Appendix C: Line-fitting results

In this appendix, we present the results of the line fit from MAD-CUBA. Tables C.1 and C.2 present the best-fit parameters from MAD-CUBA for HCN, HCO⁺, *c*-C₃H₂, H¹³CO⁺, HCO, and SO. The fit results for H₂CO and CH₃OH have already been presented in Fontani et al. (2022b). The upper-limits values are also estimated for the undetected transitions. For the (self-) absorbed lines, no best-fit parameters are given.

In Figs. C.1, C.2, and C.3, the observed spectra of the whole sample are shown with the Gaussian fits performed with MAD-CUBA for HCN, H¹³CO⁺, and SO. The plots showing the spectra of the remaining species are shown in Fontani et al. (2022) (*c*-C₃H₂, HCO⁺) and in Fontani et al. (2022b) (HCO, H₂CO, CH₃OH).

Appendix D: Molecular column densities

The derived column densities of the 39 molecular clumps for the studied molecules are within the ranges shown in Table 2. The trends of N_{tot} as a function of the galactocentric radius for all molecules are shown in Fig. D.1. A linear fit is performed for each plot, and the Pearson correlation coefficient, ρ , is calculated. As illustrated, almost constant trends and no- or weak correlations (i.e. $|\rho| \lesssim 0.2$) are found for HCN, HCO⁺, *c*-C₃H₂, H¹³CO⁺, HCO, SO, and H₂CO. A higher anti-correlation is found between CH₃OH and the galactocentric distance.

Appendix E: Galactocentric gradients of H¹³CN

The galactocentric gradients of H¹³CN fractional abundances are presented in Fig. E.1. This isotologue of HCN is characterized by a decreasing rate of ~ 114 , between the Solar circle and 24 kpc, higher than that of ¹³C (and N). A steeper decrease of this species suggests a lower formation efficiency in the OG, with respect to the inner Galaxy. It is important to highlight the contrasting behavior between HCN and HCO⁺, compared to their ¹³C isotopologues: while HCO⁺ shows a steeper decrease than H¹³CO⁺, HCN displays a shallower gradient compared to its ¹³C-bearing isotopologue.

Appendix F: Correlation between fractional abundances and between line widths

Figure F.1 shows plots to highlight possible correlations between fractional abundances and between line widths of different species. In particular, we analyzed the correlation between HCO⁺, H¹³CO⁺, HCO, H₂CO, CH₃OH (i.e., CO-product molecules), and *c*-C₃H₂, produced from the "free" carbon.

We found a high correlation between the abundances of *c*-C₃H₂ with HCO and H¹³CO⁺, with $\rho \sim 0.8 - 0.9$, and a good correlation between their line width, indicating how these two couples of molecules trace the same gas. The correlations with CH₃OH and H₂CO are less constrained, for both abundances and line widths. As said in Sect. 5.3, we would expect a low correlation coefficient between the species chemically linked to the CO and *c*-C₃H₂ because of their different formation pathways, and their weak chemical link. The correlation between these species may not result from a direct chemical link. Still, it could arise from their simultaneous formation in the star-forming region or from the similar gas they trace.

Table A.1: List of molecular clumps analyzed in this paper.

Source ^a	R.A. (J2000)	Dec (J2000)	ℓ (deg)	V_{LSR}^b (km s ⁻¹)	R_{GC}^c (kpc)	d^c (kpc)	$N_{\text{H}_2}^d$ ($\times 10^{23}$ cm ⁻²)	T_{ex}^e (K)
19383+2711				-70.2	13.2 (0.9)	14.8 (1.0)		...
19383+2711-b	19:40:22.1	27:18:33	62.58	-65.6	12.7 (0.8)	14.2 (0.9)	2.25 (0.19)	12.4 (0.8)
19423+2541	19:44:23.2	25:48:40	61.72	-72.58	13.5 (0.9)	15.3 (1.0)	2.9 (0.4)	9.9 (0.4)
19489+3030	19:50:53.2	30:38:09	66.61	-69.29	12.9 (0.8)	13.7 (0.9)	0.57 (0.06)	...
19571+3113				-66.2	12.5 (0.8)	13.0 (0.8)		...
19571+3113-b	19:59:08.5	31:21:47	68.15	-61.7	12.2 (0.8)	12.5 (0.8)	0.79 (0.08)	...
20243+3853	20:26:10.8	39:03:30	77.61	-73.21	12.8 (0.8)	11.7 (0.8)	0.77 (0.07)	...
WB89-002	20:37:22.3	47:13:54	85.41	-2.83	8.7 (0.5)	3.1 (1.6)
WB89-006				-92.3	14.5 (1.0)	12.4 (0.9)		9.8 (0.7)
WB89-006-b	20:42:58.2	47:35:35	86.27	-90.3	14.3 (1.0)	12.2 (0.9)	0.79 (0.08)	9.4 (1.0)
WB89-014	20:52:07.8	49:51:28	88.99	-96.0	14.9 (1.0)	12.5 (1.0)	0.25 (0.03)	...
WB89-031	21:04:18.0	46:53:10	88.06	-88.89	14.1 (1.0)	11.7 (0.9)	0.38 (0.03)	...
WB89-035	21:05:19.7	49:15:59	89.94	-77.56	13.1 (0.8)	10.1 (0.8)	0.39 (0.05)	11.7 (1.3)
WB89-040	21:06:50.0	50:02:09	90.68	-62.38	11.9 (0.7)	8.3 (0.7)	0.13 (0.02)	...
WB89-060	21:15:56.0	54:43:33	95.05	-83.7	13.6 (0.9)	10.1 (0.8)	1.7 (0.2)	...
WB89-076	21:24:29.0	53:45:35	95.25	-97.07	15.1 (1.1)	11.8 (0.9)	1.03 (0.10)	7.5 (1.1)
WB89-080	21:26:29.1	53:44:11	95.44	-74.1	12.8 (0.8)	8.9 (0.8)	0.51 (0.04)	9.2 (0.9)
WB89-083	21:27:47.7	54:26:58	96.08	-93.76	14.7 (1.0)	11.2 (0.9)	0.191 (0.015)	...
WB89-152	22:05:15.4	60:48:41	104.0	-88.5	14.4 (1.0)	9.8 (0.9)
WB89-283	23:32:23.8	63:33:18	114.3	-94.69	15.8 (1.1)	10.4 (0.9)	0.36 (0.04)	14.9 (1.1)
WB89-288	23:36:08.1	62:23:48	114.3	-101.0	16.8 (1.2)	11.5 (1.0)	0.54 (0.04)	...
WB89-315	00:05:53.8	64:05:17	118.0	-95.1	16.3 (1.2)	10.7 (1.0)
WB89-379	01:06:59.9	65:20:51	124.6	-89.16	16.4 (1.2)	10.2 (1.0)	1.37 (0.16)	9.3 (0.9)
WB89-380				-87.4	16.1 (1.2)	9.8 (0.9)		13 (4)
WB89-380-b	01:07:50.9	65:21:22	124.6	-86.0	15.9 (1.2)	9.6 (0.9)	5.0 (0.6)	11.4 (0.5)
WB89-391	01:19:27.1	65:45:44	125.8	-86.1	16.1 (1.2)	9.7 (0.9)	1.19 (0.13)	9.7 (0.8)
WB89-399	01:45:39.4	64:16:00	128.8	-82.15	16.0 (1.2)	9.4 (0.9)	1.75 (0.17)	11 (3)
WB89-437	02:43:29.0	62:57:08	135.3	-72.14	13.2 (0.9)	5.9 (0.7)	2.1 (0.2)	11.8 (0.4)
WB89-440	02:46:07.3	62:46:31	135.6	-71.88	15.7 (1.1)	8.6 (0.9)	0.69 (0.06)	...
WB89-501	03:52:27.6	57:48:34	145.2	-58.43	15.6 (1.1)	8.0 (0.8)	1.20 (0.13)	11.0 (1.2)
WB89-529	04:06:25.5	53:21:49	149.6	-59.8	17.8 (1.4)	10.1 (1.0)	1.17 (0.09)	...
WB89-572	04:35:58.3	47:42:58	156.9	-47.4	18.3 (1.4)	10.3 (1.1)	1.17 (0.13)	...
WB89-621	05:17:13.4	39:22:15	168.1	-25.68	13.2 (1.6)	5.0 (1.2)	1.8 (0.2)	10.3 (0.4)
WB89-640	05:25:40.7	41:41:53	167.1	-24.93	16.8 (1.3)	8.6 (0.9)	2.9 (0.2)	...
WB89-670	05:37:41.9	36:07:22	173.0	-17.65	23.4 (2.1)	15.1 (1.6)	1.34 (0.17)	...
WB89-705	05:47:47.6	35:22:01	174.7	-12.2	20.5 (1.7)	12.0 (1.3)	0.68 (0.08)	...
WB89-789	06:17:24.3	14:54:37	195.8	34.25	19.1 (1.6)	11.0 (1.1)	4.1 (0.4)	9.7 (1.0)
WB89-793	06:18:41.7	15:04:52	195.8	30.5	16.9 (1.3)	8.7 (0.9)	0.99 (0.11)	...
WB89-898	06:50:37.3	-05:21:01	217.6	63.5	15.8 (1.1)	8.4 (0.9)

Notes. ^(a) The sources labeled with a "-b" are related to secondary velocity features detected in the spectra, likely due to a second molecular clump within the telescope beam. ^(b) Local standard of rest velocities estimated from the velocity peak of the $c\text{-C}_3\text{H}_2$ $J_{K_a, K_c} = 2_{1,2} - 1_{0,1}$ line, from [Fontani et al. \(2022\)](#). For the source WB89-315, being undetected in $c\text{-C}_3\text{H}_2$, we use the V_{LSR} given in [Blair et al. \(2008\)](#). ^(c) Galactocentric distances and heliocentric distances, respectively, based on the rotation curve of [Russeil et al. \(2017\)](#), and the V_{LSR} values shown in this table. For WB89-437 and WB89-621, we assume the more accurate distances estimated through maser parallax measurements in [Hachisuka et al. \(2015\)](#). Their kinematic galactocentric distances are 15.7 and 18.9 kpc, respectively. ^(d) Derived from the NIKA2 continuum maps as described in Sect. 3.2. ^(e) Excitation temperature of CH_3OH , derived from the updated fits of the data presented in [Fontani et al. \(2022b\)](#) (see Sect. 4.1.1), adopted to fit the other species.

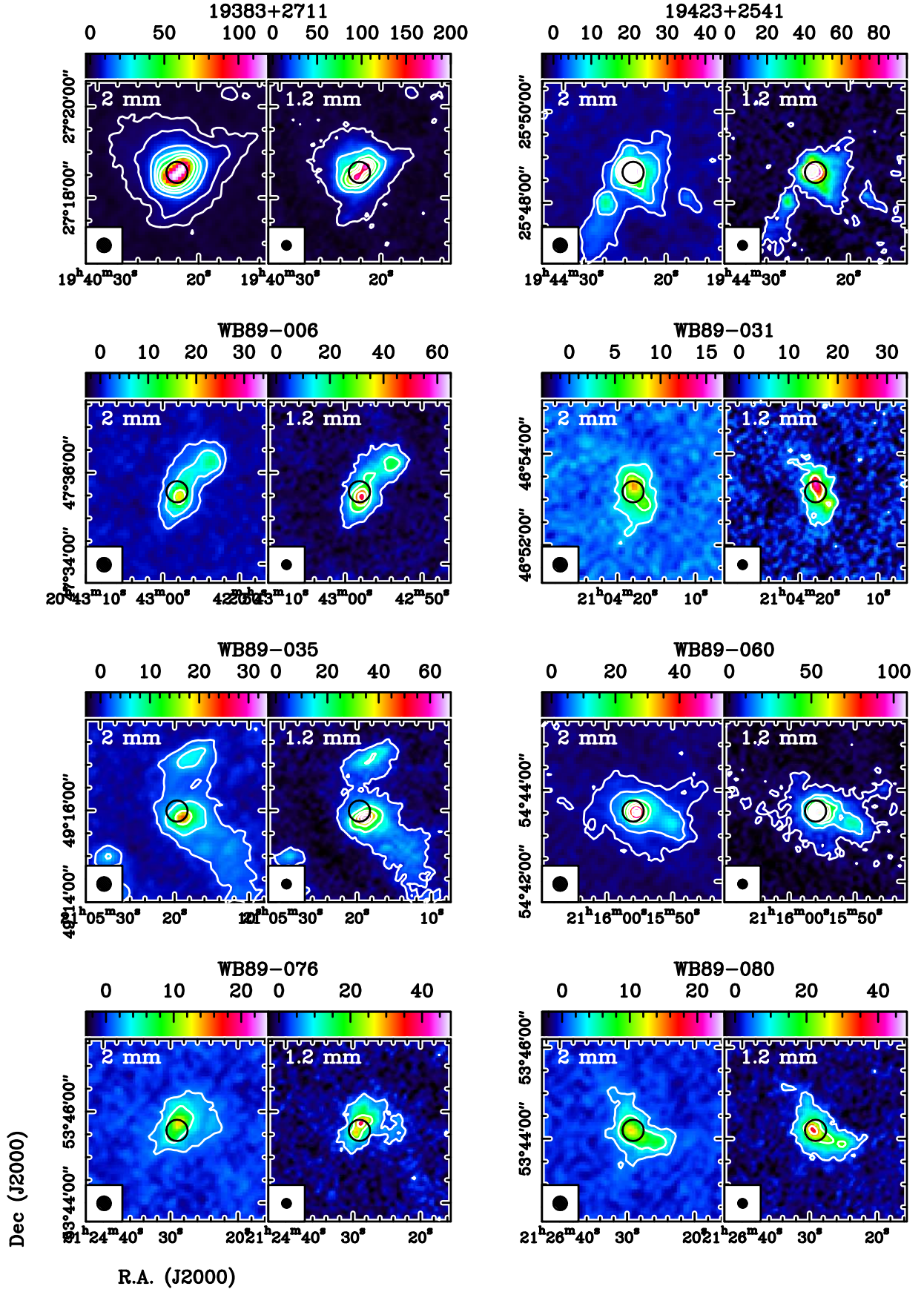


Fig. B.1: Preliminary reduced NIKA2 images (color-scale in mJy/beam) at 2.0 mm (150 GHz) and 1.2 mm (260 GHz) of 8 out of the 31 CHEMOUT sources observed (Fontani et al. in prep.). The contours start from the 5 σ rms level in each map. The NIKA2 angular resolution is shown in the bottom-left corner of each frame. The black circles on the maps represent the 28'' beam, centered on the position targeted for the molecular line observations analyzed in this paper.

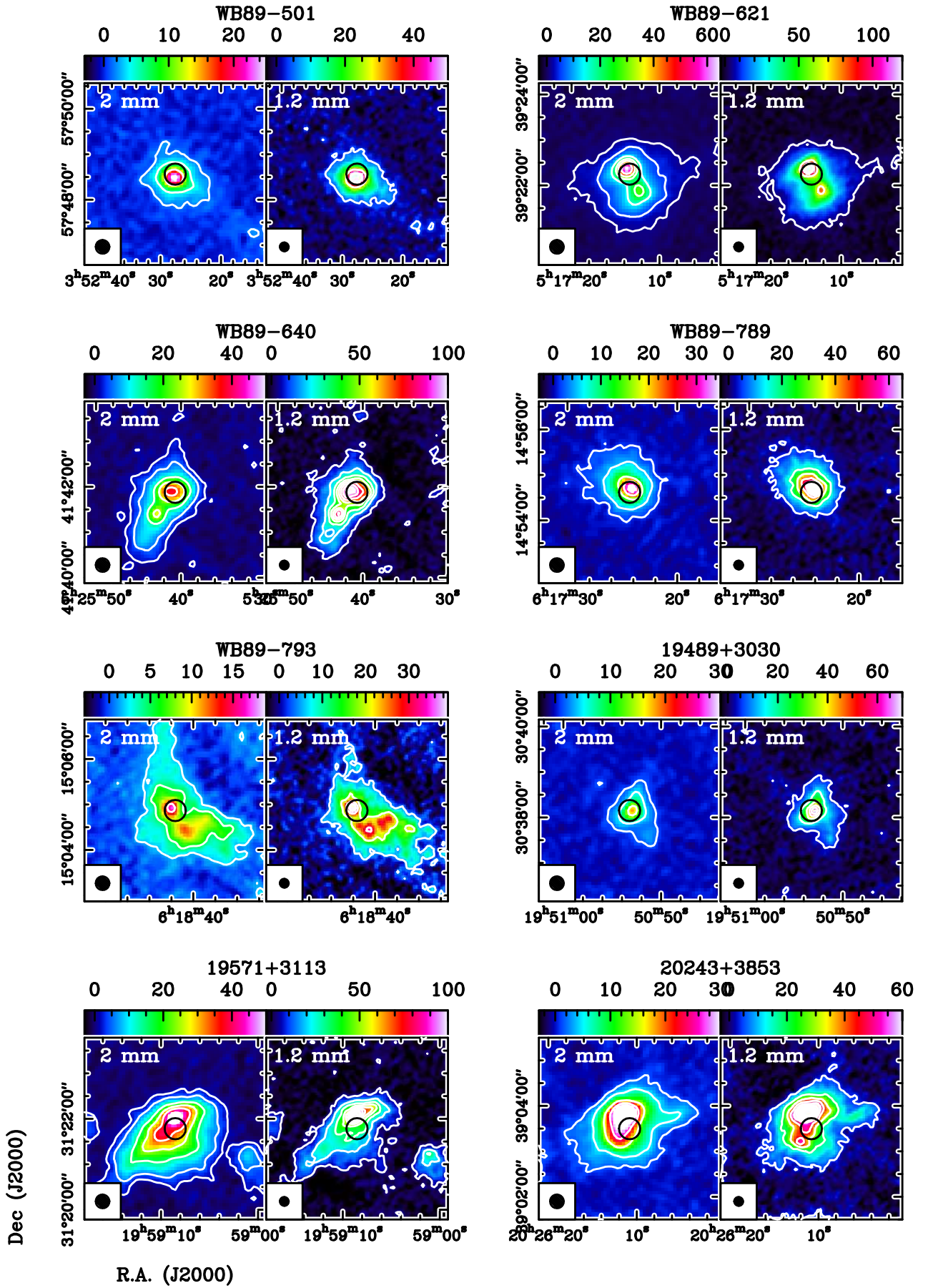


Fig. B.2: Same as Fig. B.1 for 8 additional targets.

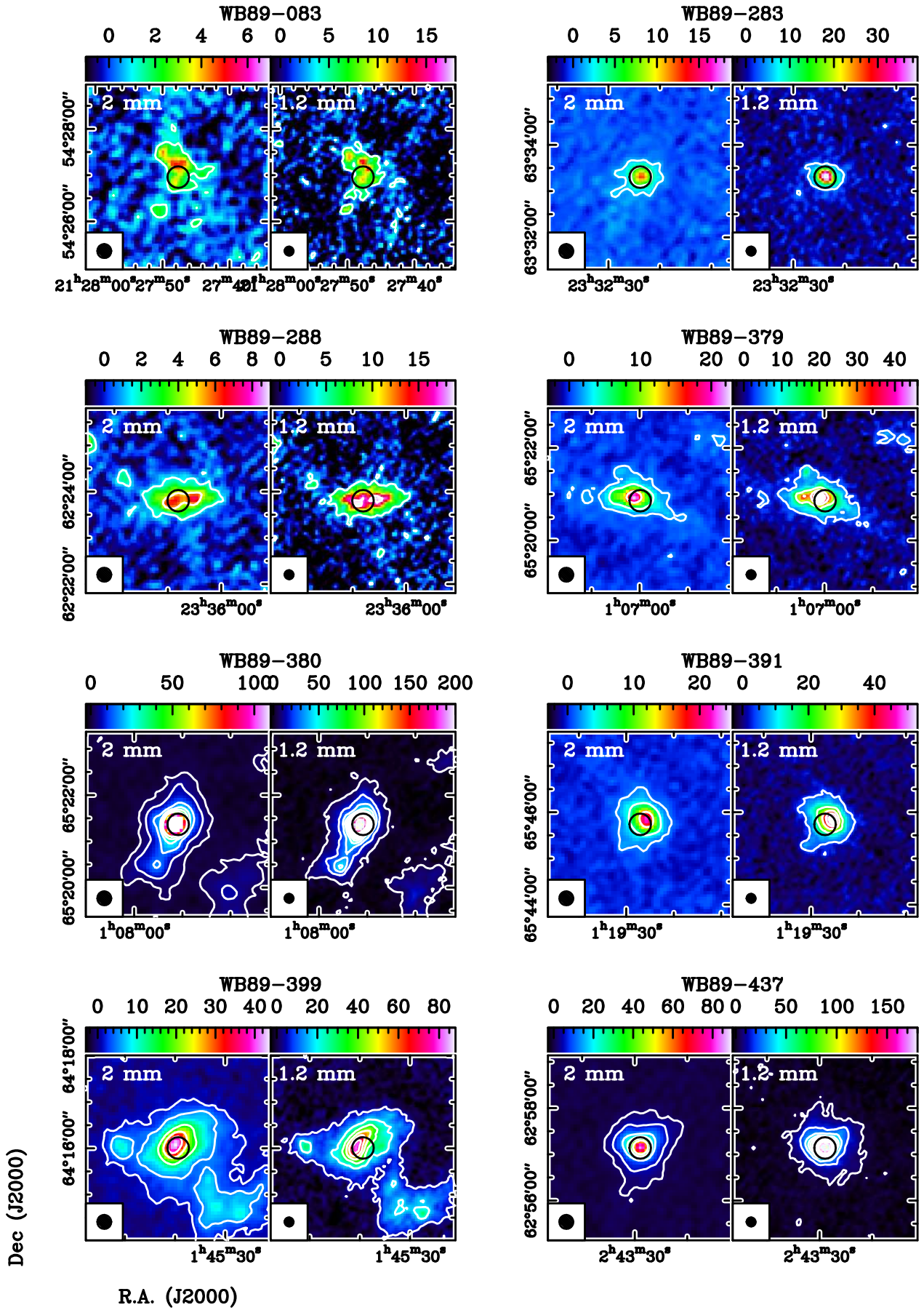


Fig. B.3: Same as Fig. B.1 for 8 additional targets.

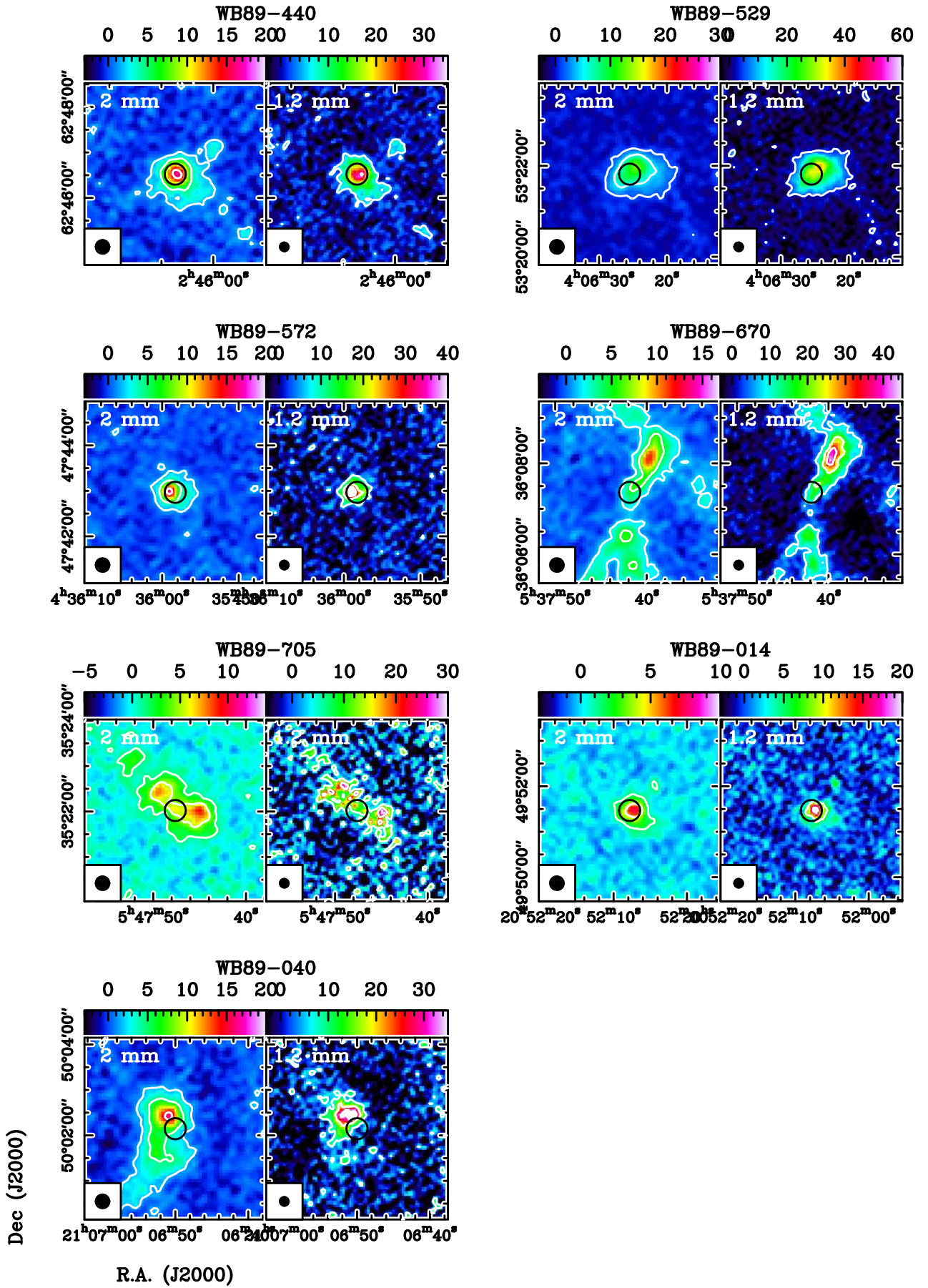


Fig. B.4: Same as Fig. B.1 for the remaining 7 targets.

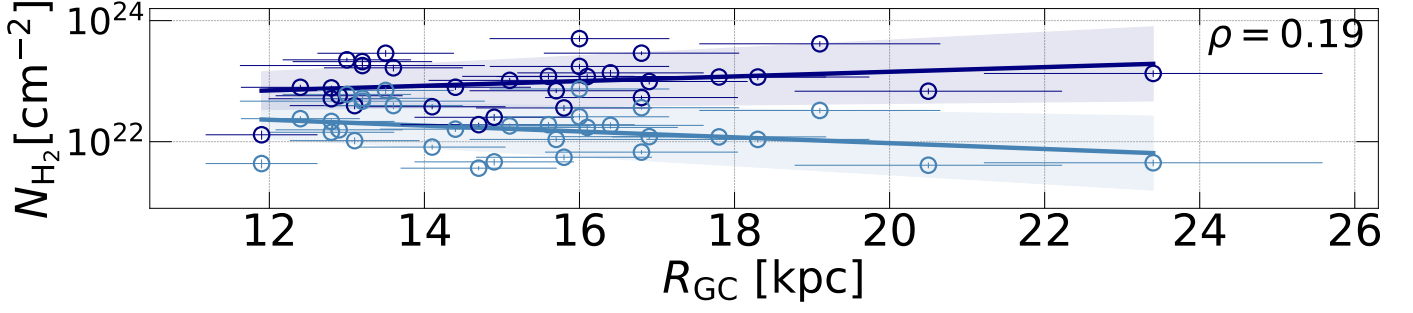


Fig. B.5: Gradients of column densities of H_2 , N_{H_2} , as a function of galactocentric radius (R_{GC}). The light blue dataset represents the column densities estimated using a constant gas-to-dust ratio ($\gamma = 100$), while the dark blue dataset shows the column densities calculated with a gas-to-dust ratio function of R_{GC} from [Giannetti et al. \(2017\)](#). Both datasets have been fitted with a linear regression. The 1σ error bars over the slope of the gradients are displayed for each fit. In the upper-right side of the plot, the Pearson correlation coefficient, ρ , is shown (only for the dark blue dataset).

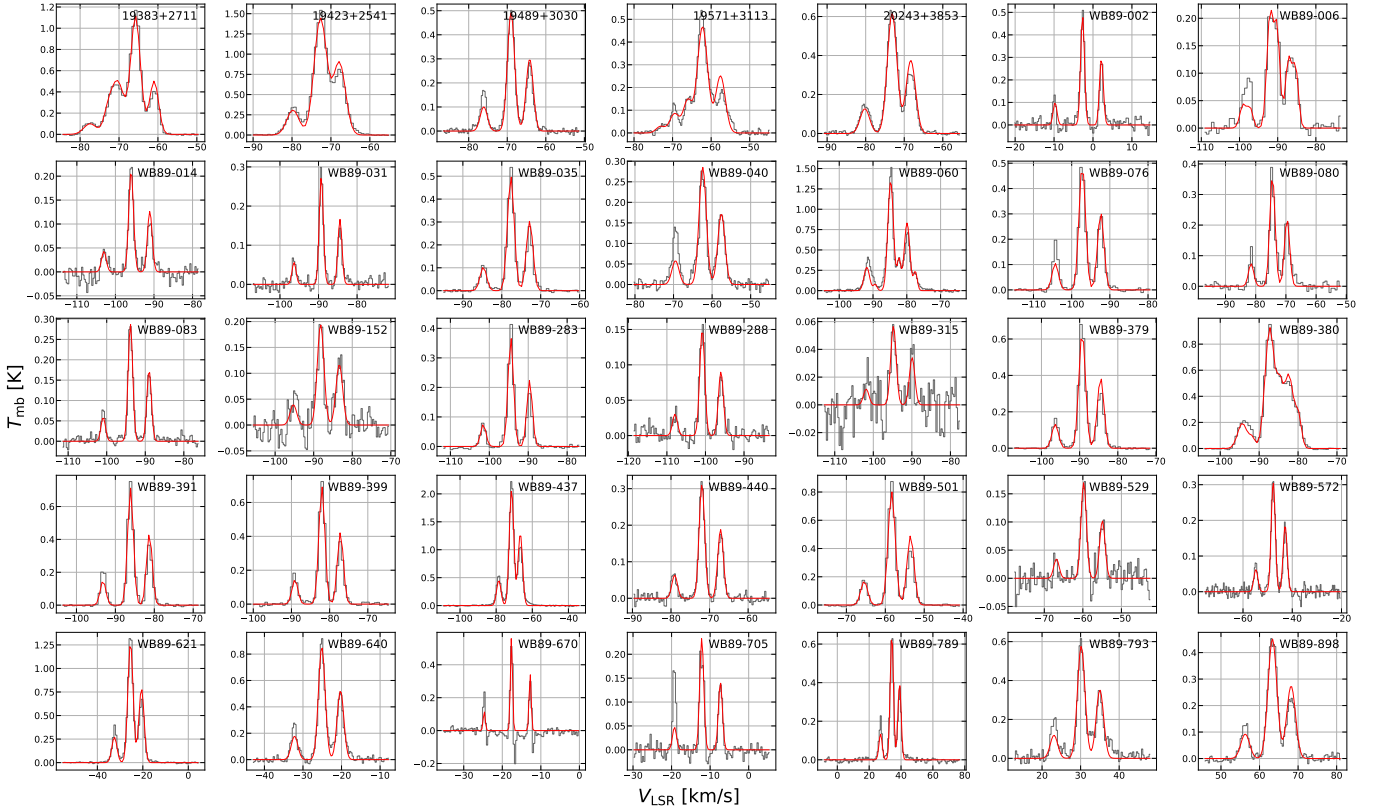


Fig. C.1: Spectra of $\text{HCN } J = 1 - 0$ ($F = 1 - 1$; $F = 2 - 1$; $F = 0 - 1$). The observed spectra (grey histograms) are superimposed on the synthetic Gaussian fits obtained with MADCUBA. The red lines represent the fit of the detected transitions, and the blue lines represent the upper limits of the non-detected transitions.

Table C.1: HCN, HCO⁺, c-C₃H₂, and H¹³CO⁺ line parameters obtained from the fitting procedure. The values of each parameter are given with the error in parentheses. If the error is not shown, the parameter was fixed during the fit. The column density values have been scaled to a 28'' beam (Sect. 3.1).

Source	HCN					HCO ⁺					c-C ₃ H ₂					H ¹³ CO ⁺					
	N_{tot} ($\times 10^{13}$ cm ⁻²)	T_{ex} (K)	V_{LSR} (km s ⁻¹)	FWHM (km s ⁻¹)	τ_{ν}	N_{tot} ($\times 10^{12}$ cm ⁻²)	T_{ex} (K)	V_{LSR} (km s ⁻¹)	FWHM (km s ⁻¹)	N_{tot} ($\times 10^{12}$ cm ⁻²)	T_{ex} (K)	V_{LSR} (km s ⁻¹)	FWHM (km s ⁻¹)	N_{tot} ($\times 10^{11}$ cm ⁻²)	T_{ex} (K)	V_{LSR} (km s ⁻¹)	FWHM (km s ⁻¹)	N_{tot} ($\times 10^{11}$ cm ⁻²)	T_{ex} (K)	V_{LSR} (km s ⁻¹)	FWHM (km s ⁻¹)
19383+2711	0.70(0.11)	10.7	-70.36(0.10)	3.8(0.2)	0.067 (0.005)	3.1(0.5)	10.7	-70.2(0.1)	4.3(0.2)	2.7(0.4)	4.4(0.4)	-70.10(0.11)	4.3(0.3)	1.0(0.3)	10.7	-70.0(0.2)	3.9(0.9)	1.0(0.3)	10.7	-70.0(0.2)	3.9(0.9)
19383+2711-b	0.90(0.12)	12.4	-65.80(0.04)	2.65(0.10)	0.092 (0.004)	4.4(0.6)	12.4	-65.80(0.04)	2.80(0.08)	1.4(0.2)	6.2(0.5)	-65.5(0.1)	3.0(0.2)	1.0(0.3)	12.4	-65.7(0.2)	2.3(0.4)	1.0(0.3)	12.4	-65.7(0.2)	2.3(0.4)
19423+2541	2.2(0.3)	9.9	-72.70(0.04)	3.70(0.08)	0.237 (0.001)	6.6(1.0)	9.9	-72.800(0.015)	3.00(0.06)	3.5(0.5)	6.1(0.4)	-72.60(0.06)	3.60(0.14)	2.2(0.4)	9.9	-72.90(0.08)	2.2(0.2)	2.2(0.4)	9.9	-72.90(0.08)	2.2(0.2)
19489+3030	0.40(0.05)	10.7	-69.00(0.02)	2.20(0.05)	0.067 (0.003)	3.0(0.3)	10.7	-69.100(0.009)	2.60(0.03)	1.4(0.2)	10.7	-69.30(0.04)	1.96(0.10)	2.7(0.4)	10.7	-69.100(0.05)	1.80(0.12)	2.7(0.4)	10.7	-69.100(0.05)	1.80(0.12)
19571+3113	0.14(0.04)	10.7	-66.1(0.2)	2.7(0.5)	0.019 (0.005)	0.9(0.2)	10.7	-65.90(0.05)	1.90(0.13)	0.60(0.15)	10.7	-66.10(0.11)	1.7(0.3)	≤ 0.2	10.7	-66.2	1.8	≤ 0.2	10.7	-66.2	1.8
19571+3113-b	0.50(0.08)	10.7	-62.40(0.08)	2.9(0.2)	0.056 (0.005)	3.1(0.4)	10.7	-62.20(0.04)	3.36(0.10)	2.6(0.4)	10.7	-61.70(0.12)	4.7(0.3)	0.50(0.12)	10.7	-62.2(0.2)	1.8	0.50(0.12)	10.7	-62.2(0.2)	1.8
20243+3853	0.70(0.08)	10.7	-73.10(0.03)	2.90(0.05)	0.084 (0.004)	3.3(0.4)	10.7	-73.20(0.04)	3.28(0.10)	1.8(0.2)	10.7	-73.20(0.05)	2.70(0.11)	1.0(0.2)	10.7	-73.6(0.2)	2.5(0.4)	1.0(0.2)	10.7	-73.6(0.2)	2.5(0.4)
WB89-002	0.20(0.03)	10.7	-2.70(0.02)	1.20(0.05)	0.066 (0.004)	0.80(0.14)	10.7	-2.50(0.05)	1.50(0.12)	0.6(0.2)	10.7	-2.80(0.07)	0.9(0.2)	0.50(0.13)	10.7	-2.60(0.04)	0.60(0.12)	0.50(0.13)	10.7	-2.60(0.04)	0.60(0.12)
WB89-006	0.20(0.06)	9.8	-92.0(0.2)	2.0(0.4)	0.032 (0.003)	1.2(0.2)	9.8	-92.20(0.02)	2.00(0.05)	0.3(0.2)	12.0(6.0)	-92.30(0.14)	1.2(0.4)	0.5(0.2)	9.8	-92.20(0.12)	1.1(0.3)	0.5(0.2)	9.8	-92.20(0.12)	1.1(0.3)
WB89-006-b	0.11(0.05)	9.4	-90.1(0.2)	1.7(0.4)	0.028 (0.003)	0.74(0.10)	9.4	-89.60(0.02)	1.50(0.05)	1.1(0.2)	7.3(0.8)	-90.30(0.04)	1.50(0.11)	1.5(0.3)	9.4	-90.40(0.06)	1.40(0.14)	1.5(0.3)	9.4	-90.40(0.06)	1.40(0.14)
WB89-014	0.12(0.02)	10.7	-95.90(0.03)	1.50(0.06)	0.028 (0.002)	1.00(0.12)	10.7	-95.90(0.02)	1.80(0.04)	0.60(0.13)	10.7	-96.00(0.09)	1.6(0.2)	≤ 0.3	10.7	-96.0	1.8	≤ 0.3	10.7	-96.0	1.8
WB89-031	0.13(0.02)	10.7	-89.30(0.02)	1.20(0.04)	0.037 (0.002)	0.70(0.13)	10.7	-89.400(0.012)	1.10(0.04)	0.70(0.15)	10.7	-88.90(0.08)	1.6(0.2)	0.30(0.11)	10.7	-89.70(0.14)	1.0(0.3)	0.30(0.11)	10.7	-89.70(0.14)	1.0(0.3)
WB89-035	0.40(0.05)	11.7	-77.70(0.02)	2.00(0.06)	0.060 (0.002)	2.0(0.2)	11.7	-77.600(0.008)	1.80(0.02)	1.5(0.2)	4.7(0.5)	-77.60(0.04)	1.50(0.08)	0.9(0.2)	11.7	-77.50(0.07)	1.5(0.2)	0.9(0.2)	11.7	-77.50(0.07)	1.5(0.2)
WB89-040	0.20(0.03)	10.7	-62.40(0.05)	2.18(0.10)	0.038 (0.004)	0.30(0.09)	10.7	-62.00(0.05)	1.8(0.2)	1.4(0.3)	10.7	-62.40(0.14)	3.2(0.3)	1.3(0.2)	10.7	-62.50(0.06)	1.40(0.14)	1.3(0.2)	10.7	-62.50(0.06)	1.40(0.14)
WB89-060
WB89-076	0.40(0.05)	7.5	-97.20(0.04)	2.00(0.08)	0.118 (0.007)	1.0(0.2)	7.5	-97.60(0.03)	1.70(0.09)	1.8(0.3)	4.9(0.4)	-97.10(0.03)	1.40(0.07)	2.1(0.3)	7.5	-97.100(0.03)	1.40(0.07)	2.1(0.3)	7.5	-97.100(0.03)	1.40(0.07)
WB89-080	0.30(0.04)	9.2	-74.50(0.05)	2.00(0.11)	0.061 (0.005)	1.0(0.3)	9.2	-74.10(0.2)	3.0(0.6)	0.8(0.2)	9.2	-74.2(0.2)	1.5(0.4)	0.8(0.2)	9.2	-74.2(0.2)	1.5(0.4)
WB89-083	0.20(0.02)	10.7	-93.800(0.014)	1.400(0.03)	0.039 (0.001)	1.4(0.2)	10.7	-93.90(0.02)	1.60(0.04)	0.68(0.10)	10.7	-93.80(0.03)	1.20(0.07)	0.40(0.09)	10.7	-93.60(0.04)	0.80(0.09)	0.40(0.09)	10.7	-93.60(0.04)	0.80(0.09)
WB89-152	0.15(0.02)	10.7	-88.20(0.06)	2.00(0.15)	0.026 (0.001)	1.3(0.2)	10.7	-88.60(0.04)	3.00(0.09)	0.5(0.2)	10.7	-88.50(0.12)	0.8(0.3)	≤ 0.6	10.7	-88.5	1.8	≤ 0.6	10.7	-88.5	1.8
WB89-283	0.30(0.04)	14.9	-94.50(0.03)	1.70(0.08)	0.032 (0.002)	1.0(0.2)	14.9	-94.40(0.01)	1.40(0.04)	0.7(0.2)	7.7(1.1)	-94.70(0.07)	2.0(0.2)	0.30(0.07)	14.9	-94.70(0.07)	1.1(0.2)	0.30(0.07)	14.9	-94.70(0.07)	1.1(0.2)
WB89-288	0.090(0.012)	10.7	-100.80(0.03)	1.50(0.07)	0.020 (0.001)	1.20(0.15)	10.7	-100.900(0.008)	1.70(0.02)	0.53(0.10)	10.7	-101.00(0.07)	1.7(0.2)	≤ 0.3	10.7	-101.0	1.8	≤ 0.3	10.7	-101.0	1.8
WB89-315	0.40(0.007)	10.7	-94.80(0.08)	1.7(0.2)	0.008 (0.001)	0.50(0.07)	10.7	-94.90(0.04)	2.07(0.10)	≤ 0.2	10.7	-94.90(0.06)	1.90(0.14)	≤ 0.4	10.7	-95.1	1.8	≤ 0.4	10.7	-95.1	1.8
WB89-379	0.50(0.06)	9.3	-89.30(0.03)	2.00(0.08)	0.108 (0.006)	0.7(0.2)	9.3	-89.50(0.03)	1.40(0.12)	0.70(0.11)	6.4	-89.20(0.06)	1.90(0.14)	1.0(0.2)	9.3	-89.100(0.05)	1.60(0.12)	1.0(0.2)	9.3	-89.100(0.05)	1.60(0.12)
WB89-380	1.1(0.2)	13.0	-87.30(0.05)	2.80(0.11)	0.099 (0.003)	5.1(0.7)	13.0	-87.40(0.05)	2.60(0.11)	1.6(1.3)	11.0(8.0)	-87.4(0.3)	2.8(0.8)	2.3(0.5)	13.0	-86.1(0.2)	4.8(0.5)	2.3(0.5)	13.0	-86.1(0.2)	4.8(0.5)
WB89-380-b	0.30(0.07)	11.4	-84.70(0.09)	1.8(0.2)	0.047 (0.003)	2.3(0.4)	11.4	-84.10(0.07)	2.2(0.2)	3.0(2.0)	5.0(1.2)	-86.0(1.0)	4.0(0.6)	0.7(0.2)	11.4	-85.200(0.07)	1.1(0.2)	0.7(0.2)	11.4	-85.200(0.07)	1.1(0.2)
WB89-391	0.50(0.06)	9.7	-86.10(0.03)	1.70(0.07)	0.114 (0.006)	2.1(0.2)	9.7	-86.20(0.02)	1.80(0.03)	2.3(0.3)	3.7	-86.10(0.03)	1.60(0.08)	0.80(0.15)	9.7	-86.100(0.07)	1.4(0.2)	0.80(0.15)	9.7	-86.100(0.07)	1.4(0.2)
WB89-399	0.50(0.06)	11.0	-82.00(0.02)	1.80(0.05)	0.092 (0.003)	3.4(0.4)	11.0	-81.900(0.012)	2.00(0.03)	2.6(0.4)	4.5(0.4)	-82.20(0.04)	2.20(0.09)	≤ 0.4	11.0	82.15	1.8	≤ 0.4	11.0	82.15	1.8
WB89-437	2.6(0.3)	11.8	-71.50(0.04)	2.80(0.08)	0.270 (0.015)	9.5(1.0)	11.8	-71.300(0.008)	2.70(0.02)	2.5(0.4)	4.2	-72.10(0.07)	3.0(0.2)	3.3(0.5)	11.8	-71.600(0.05)	2.40(0.11)	3.3(0.5)	11.8	-71.600(0.05)	2.40(0.11)
WB89-440	0.20(0.02)	10.7	-72.00(0.02)	1.70(0.04)	0.042 (0.001)	3.2(0.3)	10.7	-71.900(0.009)	2.00(0.02)	1.2(0.2)	10.7	-71.90(0.05)	1.60(0.12)	≤ 0.3	10.7	-71.88	1.8	≤ 0.3	10.7	-71.88	1.8
WB89-501	0.70(0.09)	11.0	-58.40(0.03)	2.10(0.07)	0.107 (0.005)	3.0(0.4)	11.0	-58.20(0.04)	2.10(0.09)	1.6(0.2)	4.7	-58.40(0.04)	2.16(0.10)	0.8(0.2)	11.0	-58.60(0.15)	2.1(0.3)	0.8(0.2)	11.0	-58.60(0.15)	2.1(0.3)
WB89-529	0.11(0.02)	10.7	-59.80(0.04)	1.60(0.09)	0.023 (0.002)	2.1(0.3)	10.7	-59.70(0.02)	1.80(0.05)	0.8(0.2)	10.7	-59.8(0.2)	1.9(0.4)	≤ 0.5	10.7	-59.8	1.8	≤ 0.5	10.7	-59.8	1.8
WB89-572	0.20(0.03)	10.7	-47.70(0.02)	2.00(0.04)	0.041 (0.002)	1.10(0.14)	10.7	-47.80(0.02)	2.40(0.06)	0.40(0.12)	10.7	-47.42(0.10)	1.0(0.2)	0.5(0.2)	10.7	-47.20(0.3)	1.6(0.7)	0.5(0.2)	10.7	-47.20(0.3)	1.6(0.7)
WB89-621	1.4(0.2)	10.3	-25.40(0.04)	2.60(0.08)	0.0194 (0.010)	4.0(0.4)	10.3	-25.63(0.01)	3.10(0.03)	0.80(0.13)	6.7	-25.70(0.06)	2.00(0.15)	2.6(0.4)	10.3	-25.100(0.04)	2.22(0.10)	2.6(0.4)	10.3	-25.100(0.04)	2.22(0.10)
WB89-640	0.70(0.08)	10.7	-25.10(0.02)	2.00(0.05)	0.119 (0.006)	1.1(0.3)	10.7	-25.10(0.03)	1.10(0.09)	2.3(0.4)	10.7	-24.90(0.09)	2.4(0.2)	3.9(0.7)	10.7	-25.400(0.09)	2.6(0.2)	3.9(0.7)	10.7	-25.400(0.09)	2.6(0.2)
WB89-670	0.14(0.03)	10.7	-17.60(0.04)	0.60(0.08)	0.078 (0.011)	1.2(0.2)	10.7	-17.68(0.01)	0.90(0.02)	1.8(0.4)	7.8	-17.70(0.04)	0.67(0.10)	2.1(0.6)	10.7	-17.70(0.06)	0.60(0.12)	2.1(0.6)	10.7	-17.70(0.06)	0.60(0.12)
WB89-705	0.11(0.02)	10.7	-12.20(0.05)	1.20(0.13)	0.031 (0.005)	0.60(0.11)	10.7	-12.20(0.05)	1.40(0.12)	1.3(0.2)	8.2	-12.200(0.013)	0.70(0.03)	1.9(0.3)	10.7	-12.200(0.02)	0.60(0.04)	1.9(0.3)	10.7	-12.200(0.02)	0.60(0.04)
WB89-789	0.60(0.08)	9.7	34.20(0.04)	2.40(0.08)	0.102 (0.005)	3.9(0.4)	9.7	34.200(0.015)	3.10(0.04)	1.4(0.3)	7.1(1.0)	34.30(0.06)	1.90(0.15)	3.3(0.5)	9.7	34.200(0.05)	2.00(0.12)	3.3(0.5)	9.7	34.200(0.05)	2.00(0.12)
WB89-793	0.50(0.07)	10.7	30.20(0.04)	2.30(0.09)	0.079 (0.006)	2.3(0.3)	10.7	29.80(0.02)	1.70(0.05)	1.4(0.4)	10.7	30.5(0.2)	2.1(0.4)	2.5(0.4)	10.7	30.20(0.06)	1.8(0.2)	2.5(0.4)	10.7	30.20(0.06)	1.8(0.2)
WB89-898	0.50(0.06)	10.7	63.30(0.03)	2.70(0.06)	0.061 (0.003)	2.2(0.3)	10.7	63.30(0.03)	3.20(0.07)	1.2(0.3)	10.7	63.50(0.14)	2.6(0.3)	≤ 0.3	10.7	63.5	1.8	≤ 0.3	10.7	63.5	1.8

Notes. ^(a) Optical depth estimated from the hyperfine structure of HCN, by MADCUBA. The values are referring to the strongest line, i.e., HCN $J = 1 - 0$, $F = 2 - 1$ transition, at 88.63185 GHz, and they represent lower limit values due to the unknown source sizes and the assumed temperatures. The error shown is estimated by MADCUBA.

Table C.2: Same as Table C.1 for HCO, SO, H₂CO, and CH₃OH.

Source	HCO					SO					H ₂ CO					CH ₃ OH				
	N_{tot} ($\times 10^{13}$ cm ⁻²)	T_{ex} (K)	V_{LSR} (km s ⁻¹)	FWHM (km s ⁻¹)	N_{rot} ($\times 10^{13}$ cm ⁻²)	T_{ex} (K)	V_{LSR} (km s ⁻¹)	FWHM (km s ⁻¹)	N_{rot} ($\times 10^{14}$ cm ⁻²)	T_{ex} (K)	V_{LSR} (km s ⁻¹)	FWHM (km s ⁻¹)	θ_{S} ($''$)	N_{rot} ($\times 10^{13}$ cm ⁻²)	T_{ex} (K)	V_{LSR} (km s ⁻¹)	FWHM (km s ⁻¹)	θ_{S} ($''$)		
19383+2711	0.40(0.12)	10.7	-69.7(0.3)	3.9(0.6)	0.32(0.10)	10.7	-69.9(0.5)	3.6	0.11(0.04)	42.0(8.0)	-70.40(0.06)	4.0(0.2)	...	≤ 0.1	10.7	-70.2	1.9	...		
19383+2711-b	0.20(0.11)	12.4	-65.7(0.5)	3.5(0.9)	0.50(0.12)	12.4	-66.0(0.2)	2.6(0.5)	0.20(0.03)	36.0(2.0)	-65.700(0.015)	2.50(0.04)	...	1.3(0.2)	12.4(0.8)	-65.90(0.04)	2.0(0.1)	...		
19423+2541	0.40(0.06)	9.9	-72.50(0.08)	3.1(0.2)	2.4(0.3)	9.9	-73.00(0.06)	3.10(0.14)	0.60(0.12)	41.0(3.0)	-72.60(0.02)	4.00(0.05)	35	4.6(0.7)	9.9(0.4)	-72.40(0.06)	4.00(0.13)	28		
19489+3030	≤ 0.1	10.7	-69.29	2.1	0.30(0.11)	10.7	-69.5(0.2)	1.8(0.6)		
19571+3113	0.30(0.12)	10.7	-65.5(0.6)	4.8(1.3)	≤ 0.1	10.7	-66.2	2.0		
19571+3113-b	0.30(0.11)	10.7	-61.1(0.4)	3.4(0.7)	≤ 0.1	10.7	-61.7	2.0		
20243+3853	0.30(0.05)	10.7	-73.10(0.06)	2.30(0.13)	0.50(0.13)	10.7	-73.5(0.2)	3.0(0.5)		
WB89-002	0.20(0.05)	10.7	-2.80(0.06)	0.90(0.15)	≤ 0.3	10.7	-2.83	2.0		
WB89-006	≤ 0.1	9.8	-92.3	2.1	0.24(0.10)	9.8	-92.0	2.0	0.053(0.010)	29.0(2.0)	-92.10(0.05)	1.70(0.07)	...	1.1(0.3)	9.8(0.7)	-92.00(0.09)	1.6(0.2)	...		
WB89-006-b	0.07(0.04)	9.4	-90.5(0.3)	1.2(0.7)	≤ 0.2	9.4	-90.3	2.0	0.040(0.008)	23.0(2.0)	-90.30(0.06)	1.92(0.10)	...	0.7(0.2)	9.4(1.0)	-90.30(0.09)	1.3(0.2)	...		
WB89-014	≤ 0.1	10.7	-96.0	2.1	≤ 0.2	10.7	-96.0	2.0		
WB89-031	0.12(0.03)	10.7	-88.8(0.2)	1.8(0.4)	≤ 0.1	10.7	-88.89	2.0		
WB89-035	0.14(0.05)	11.7	-77.60(0.08)	1.3(0.2)	0.80(0.13)	11.7	-78.10(0.05)	1.70(0.12)	0.14(0.03)	32.0(3.0)	-77.60(0.02)	2.40(0.05)	32	1.2(0.2)	12.0(1.3)	-77.70(0.06)	2.40(0.14)	35		
WB89-040	0.30(0.05)	10.7	-62.30(0.08)	2.1(0.2)	0.70(0.14)	10.7	-62.20(0.08)	1.6(0.2)		
WB89-060	≤ 0.1	10.7	-83.7	2.2	3.6(0.5)	10.7	-84.00(0.05)	2.50(0.12)		
WB89-076	0.06(0.02)	7.5	-97.00(0.15)	1.3(0.3)	1.7(0.2)	7.5	-97.30(0.02)	1.30(0.05)	0.060(0.011)	28.0(3.0)	-97.30(0.02)	1.90(0.05)	98	1.7(0.5)	7.5(1.1)	-97.30(0.06)	1.50(0.14)	33		
WB89-080	0.07(0.02)	9.2	-73.90(0.09)	0.7	0.80(0.14)	9.2	-74.40(0.04)	1.00(0.09)	0.12(0.03)	30.0(5.0)	-74.50(0.03)	1.70(0.07)	32	1.4(0.3)	9.2(0.9)	-74.40(0.06)	1.90(0.14)	32		
WB89-083	0.10(0.03)	10.7	-93.70(0.11)	1.4(0.3)	≤ 0.1	10.7	-93.76	2.0		
WB89-152	≤ 0.1	10.7	-88.5	2.1	≤ 0.3	10.7	-88.5	2.0		
WB89-283	0.20(0.05)	14.9	-94.50(0.14)	2.6(0.3)	0.30(0.09)	14.9	-94.7(0.3)	2.5(0.7)	0.12(0.02)	35.0(4.0)	-94.50(0.02)	1.60(0.04)	36	1.1(0.2)	15.0(1.1)	-94.40(0.03)	1.40(0.07)	32		
WB89-288	0.20(0.04)	10.7	-100.60(0.07)	1.4(0.2)	≤ 0.2	10.7	-101.1	2.1		
WB89-315	≤ 0.1	10.7	-95.1	2.1	≤ 0.2	10.7	-95.1	2.0		
WB89-379	0.20(0.03)	9.3	-89.20(0.09)	2.3(0.2)	0.4(0.1)	9.3	-89.20(0.11)	1.5(0.3)	0.13(0.02)	33.0(2.0)	-89.400(0.011)	1.80(0.03)	34	1.6(0.3)	9.3(0.9)	-89.30(0.05)	1.70(0.11)	30		
WB89-380	0.60(0.08)	13.0	-86.60(0.06)	2.90(0.13)	1.1(0.2)	13.0	-86.7(0.2)	4.1(0.4)	0.20(0.07)	39.0(8.0)	-87.6(0.2)	2.3(0.2)	...	0.20(0.13)	13.0(4.0)	-88.4(0.1)	1.0(0.3)	...		
WB89-380-b	≤ 0.1	11.4	-86.0	2.1	0.40(0.12)	11.4	-85.20(0.06)	1.0(0.2)	0.15(0.06)	22.0(2.0)	-85.6(0.3)	2.8(0.3)	...	2.5(0.4)	11.4(0.5)	-86.30(0.08)	3.0(0.2)	...		
WB89-391	0.30(0.04)	9.7	-85.90(0.04)	1.71(0.10)	1.10(0.15)	9.7	-86.00(0.03)	1.30(0.06)	0.090(0.015)	25.0(2.0)	-86.00(0.02)	1.60(0.04)	49	1.7(0.3)	9.7(0.8)	-85.90(0.03)	1.40(0.07)	29		
WB89-399	0.40(0.07)	11.0	-81.80(0.09)	2.0(0.2)	≤ 0.2	11.0	-82.15	2.0	0.11(0.03)	46.0(7.0)	-82.20(0.02)	1.60(0.04)	128	0.30(0.09)	11.0(3.0)	-82.20(0.05)	1.00(0.13)	56		
WB89-437	0.20(0.05)	11.8	-71.8(0.2)	2.9(0.4)	3.6(0.5)	11.8	-71.60(0.04)	2.81(0.10)	1.00(0.15)	33.0(2.0)	-71.40(0.02)	2.80(0.04)	21	11.0(1.4)	11.8(0.4)	-71.60(0.03)	3.00(0.07)	22		
WB89-440	0.40(0.06)	10.7	-71.70(0.04)	1.66(0.10)	≤ 0.2	10.7	-71.88	2.0		
WB89-501	0.30(0.05)	11.0	-58.30(0.07)	2.1(0.2)	0.60(0.11)	11.0	-58.50(0.06)	1.90(0.15)	0.20(0.04)	34.0(3.0)	-58.50(0.02)	2.00(0.04)	30	1.9(0.4)	11.0(1.2)	-58.60(0.05)	1.70(0.11)	31		
WB89-529	0.30(0.05)	10.7	-59.50(0.07)	1.3(0.2)	≤ 0.3	10.7	-59.8	2.0		
WB89-572	≤ 0.1	10.7	-47.4	2.2	0.7(0.2)	10.7	-47.9(0.1)	1.7(0.2)		
WB89-621	0.14(0.03)	10.3	-25.70(0.14)	2.2(0.3)	5.2(0.7)	10.3	-25.30(0.03)	2.00(0.07)	0.40(0.07)	25.0(2.0)	-25.30(0.03)	2.40(0.06)	38	10.0(1.4)	10.3(0.4)	-25.40(0.02)	1.70(0.05)	26		
WB89-640	0.80(0.11)	10.7	-25.10(0.06)	2.50(0.14)	1.0(0.2)	10.7	-25.20(0.12)	1.8(0.3)		
WB89-670	≤ 0.1	10.7	-17.65	2.1	≤ 0.2	10.7	-17.65	2.0		
WB89-705	0.07(0.02)	10.7	-11.90(0.08)	0.7(0.2)	0.50(0.07)	10.7	-12.20(0.02)	0.60(0.04)		
WB89-789	0.30(0.06)	9.7	34.20(0.07)	1.9(0.2)	0.9(0.2)	9.7	34.1(0.2)	2.8(0.4)	0.30(0.11)	44.0(8.0)	34.20(0.03)	2.10(0.07)	22	1.5(0.3)	9.7(1.0)	34.10(0.05)	2.00(0.13)	32		
WB89-793	≤ 0.1	10.7	30.5	2.1	1.2(0.3)	10.7	30.20(0.07)	1.3(0.2)		
WB89-898	0.12(0.04)	10.7	63.4(0.3)	2.0	0.8(0.2)	10.7	63.2(0.2)	2.5(0.5)		

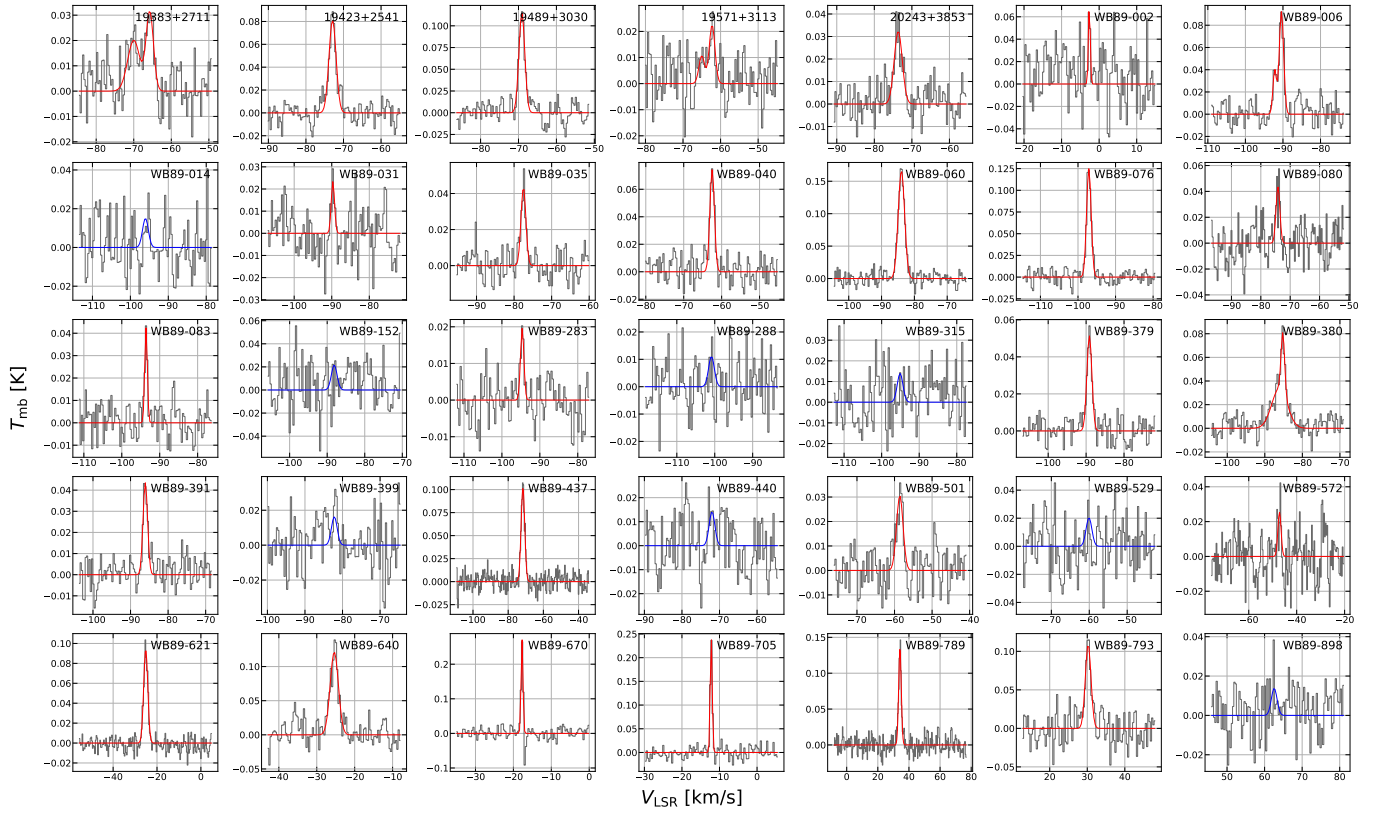


Fig. C.2: Same as Fig. C.1 for $\text{H}^{13}\text{CO}^+ J = 1 - 0$.

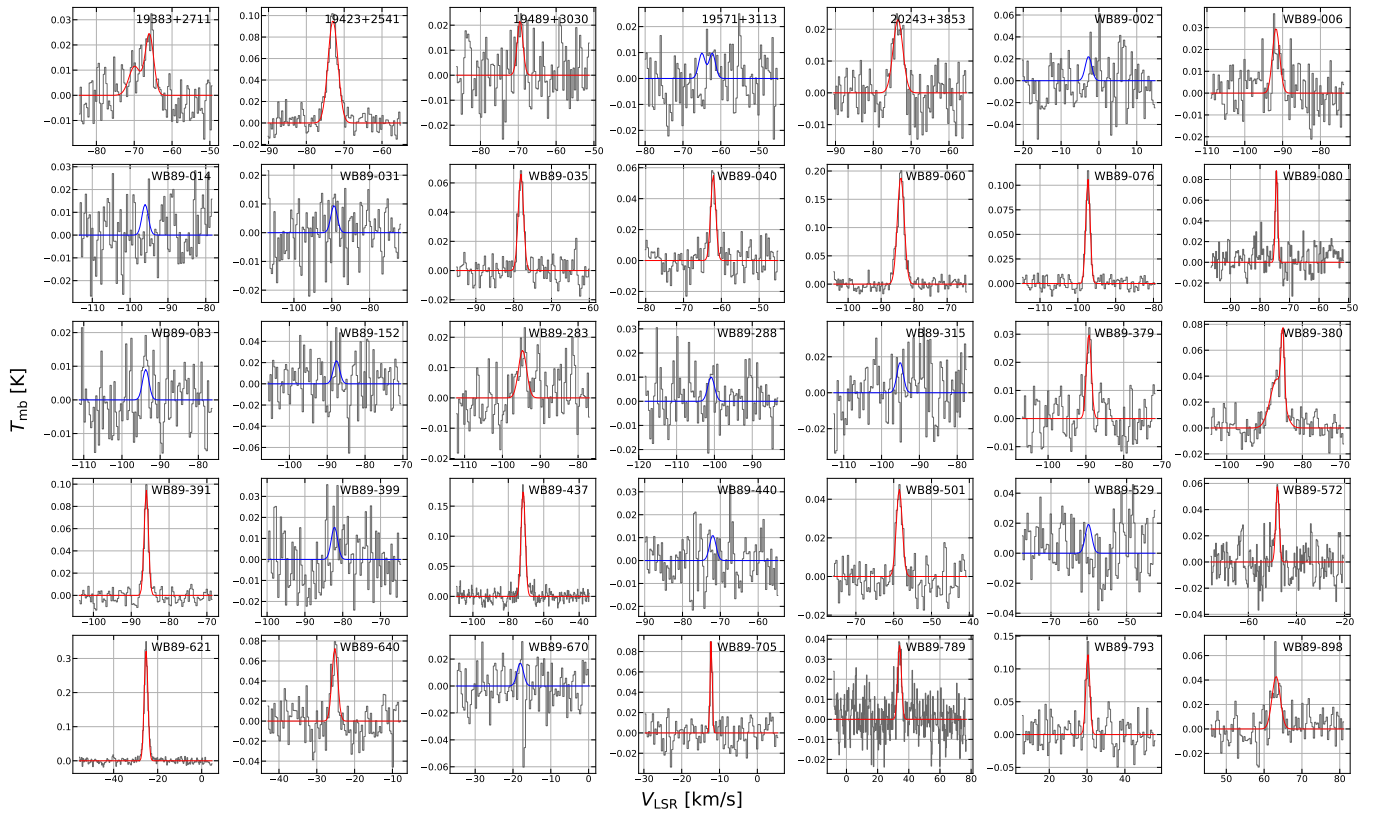


Fig. C.3: Same as Fig. C.1 for $\text{SO } N = 2 - 1, J = 2 - 1$.

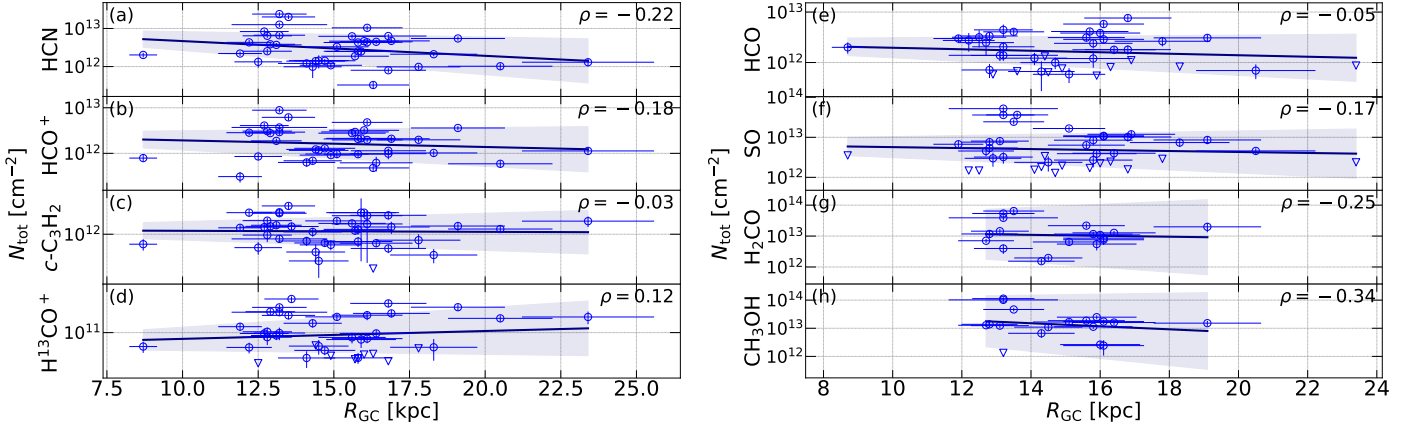


Fig. D.1: Galactocentric gradients of column densities, N_{tot} . The plots show the trends for HCN (a), HCO^+ (b), $c\text{-C}_3\text{H}_2$ (c), H^{13}CO^+ (d), HCO (e), SO (f), H_2CO (g), and CH_3OH (h) as a function of galactocentric radius (R_{GC}). The upper limit values are represented with triangles. The dark blue lines represent the linear regressions computed over the datasets. In the upper-right side of each subplot, the Pearson correlation coefficient, ρ , is shown.

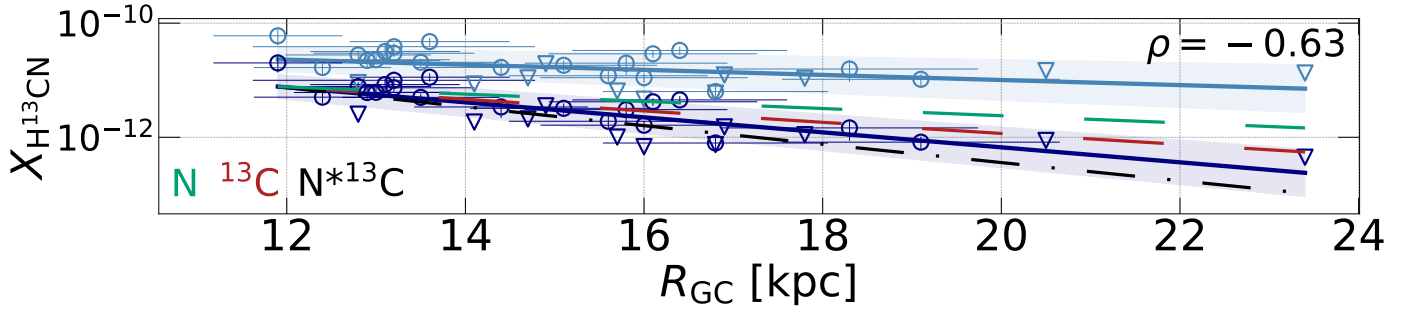


Fig. E.1: Galactocentric gradients of fractional abundances w.r.t. H_2 , X_{mol} , of H^{13}CN . The light blue data represent the abundances calculated using a constant gas-to-dust ratio ($\gamma = 100$), while the dark blue data illustrate those estimated using a non-constant gas-to-dust ratio ($\gamma = \gamma(R_{\text{GC}})$) from [Giannetti et al. 2017](#)). For both datasets, the linear regression results are shown as the light blue and dark blue lines, respectively. The 1σ error bars over the slope of the gradients are displayed for each molecular fit. The upper limit values are represented with triangles. The gradients of the elemental abundances of carbon (^{13}C) and nitrogen (N), as reported by [Méndez-Delgado et al. \(2022\)](#), are plotted as dashed lines. The product of the parent elements of the species is represented by a black dash–dot line. All the elemental trends are plotted shifted to the start of the molecular gradients estimated with $\gamma(R_{\text{GC}})$ for reference to allow comparison of their slopes with the linear fit of the molecular abundances. In the upper-right side of each plot, the Pearson correlation coefficient, ρ , is shown (estimated only for the abundances estimated using the non-constant gas-to-dust ratio).

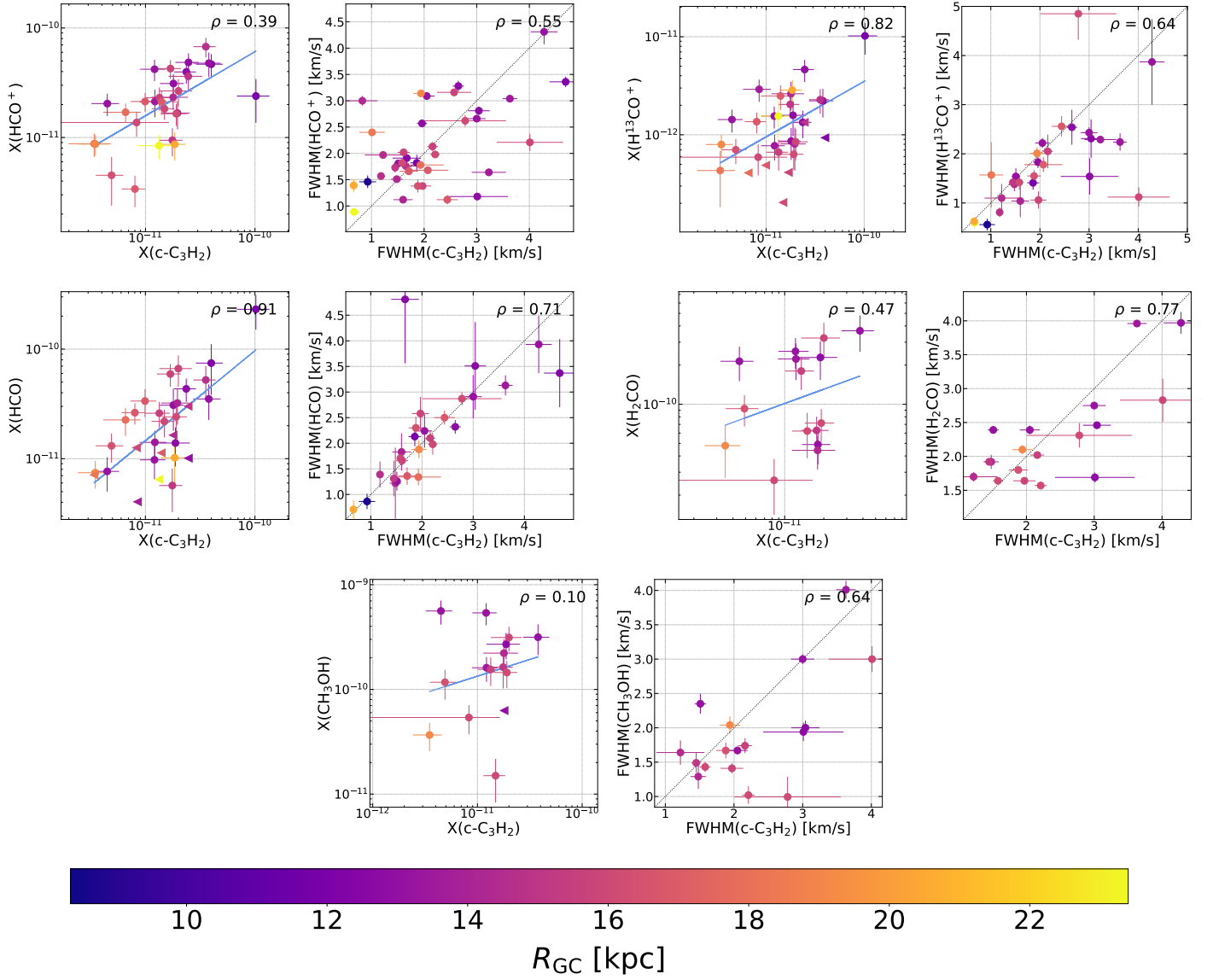


Fig. F.1: Correlation plots between fractional abundances and between line widths, of CO-related species (i.e., HCO^+ , H^{13}CO^+ , HCO , H_2CO , and CH_3OH) and $c\text{-C}_3\text{H}_2$. A linear fit is performed for the abundance plots. The upper limit values are represented with triangles. The Pearson correlation coefficient, ρ , is estimated and shown in all the plots (top-right). Galactocentric radius is color-coded for each source with the color scale on the bottom.